Theory of Mesophases of Triblock Comb-Shaped Copolymers: Effects of Dead Zones and Bridging

Ekaterina B Zhulina, Ivan V Mikhailov, Oleg V. Borisov

Macromolecules

pubs.acs.org/Macromolecules Article

Theory of Mesophases of Triblock Comb-Shaped Copolymers: Effects of Dead Zones and Bridging

Ekaterina B. Zhulina, Ivan V. Mikhailov, and Oleg V. Borisov*

Cite This: https://doi.org/10.1021/acs.macromol.2c00418 Read Online

ACCESS | Metrics & More | Article Recommendations | Supporting Information

ABSTRACT: A theory describing the equilibrium morphology and structural properties of solvent-free mesophases of *ABA* triblock copolymers comprised of comblike blocks is developed using a strong-stretching self-consistent field (SS-SCF) analytical approach with architecture-dependent parameters of the molecular potential. Morphological phase diagrams are constructed by implementing a two-layer model of convex solvent-free brushes which enables us to account for the effect of "dead zones" on binodals separating regions of thermodynamic stability of spherical, cylindrical, and lamellar mesophases. Fractions of the middle comblike *B* blocks forming bridges and loops between neighboring *A* domains are calculated for all of the morphologies as a function of the architectural parameters of the blocks. These analytical calculations are supplemented by numerical Scheutjens−Fleer self-consistent field (SF-SCF) simulations of convex solvent-free brushes of comblike polymers that mimic the matrix in the *ABA* triblock copolymer mesophases. The predicted domain sizes and interdomain distances are compared to experimental data.

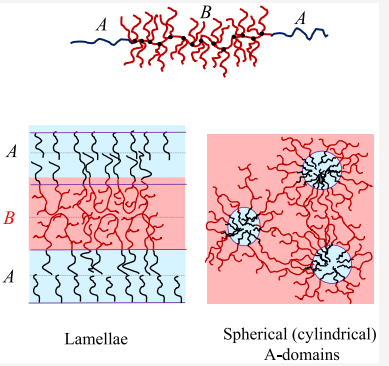

1. INTRODUCTION

Self-assembling block copolymers give rise to brushlike structures in melts and solutions. Solvated and dry brushes emerge, e.g., upon self-assembly of block copolymers with linear and branched blocks in selective solvents[1−5] or in the melt state.[6−15] Microphase-segregated bulk morphologies of block copolymers comprising branched blocks exhibit mechanical properties resembling biological tissues.[16−19] Incorporation of comblike or bottlebrush blocks enables adjusting the properties of nanostructured materials through controlled variation of the grafting density or/and the polymerization degree of the grafts without changing their chemical nature. This control is assured by well-elaborated and robust techniques developed for the synthesis of comblike polymers and molecular brushes. Due to potential applications in (bio)engineering and nanomedicine,[5,20−22] brushes of branched polymers with diverse topologies have become a subject of intense theoretical investigation during the past decade.[23−30]

The structural properties of brushes formed by end-tethered macromolecules with various branched architectures (e.g., regular dendrons, arm-tethered stars, macrocycle-containing polymers, etc.) can be described via analytical theories invoking architecture-dependent molecular potential. The pioneering study of Pickett[23] demonstrated the parabolic nature of the self-consistent molecular potential acting in brushes formed by root-tethered regular dendrons and paved the way to extension of this approach to other molecular architectures.[31−35]

Application of the parabolic potential framework to brushes of branched polymers has a number of evident advantages. It allows for closed analytical expressions for polymer density distributions in both undeformed and compressed brushes under various solvent conditions[34] and formulation of their elastic response to deformation.[35] It also specifies the free energy for both solvated and solvent-free brushes that facilitates the analysis of micellization in solutions[33] and microphase segregation in melts.[36] On the other hand, the parabolic potential framework has its drawbacks as it specifies only the most probable state of the system and, importantly, ignores the possible presence of dead zones (regions depleted of chain free ends). The latter could arise for certain architectures of the tethered chains in both planar and nonplanar geometries and perturb the parabolic shape of the molecular potential. In this case, the parabolic self-consistent field (SCF) potential should be considered as an approximation whose accuracy could be evaluated via alternative methods, e.g., numerical SCF modeling accounting for dead zones.

In our recent study,[36] we applied the parabolic potential framework (SS-SCF) to study microphase-segregated melts of *AB* diblock copolymers with comblike and bottlebrush blocks. Comblike and bottlebrush polymers were distinguished based on the conformational state of their backbones in melts. While

Received: April 26, 2022
Revised: May 29, 2022

https://doi.org/10.1021/acs.macromol.2c00418
Macromolecules XXXX, XXX, XXX−XXX

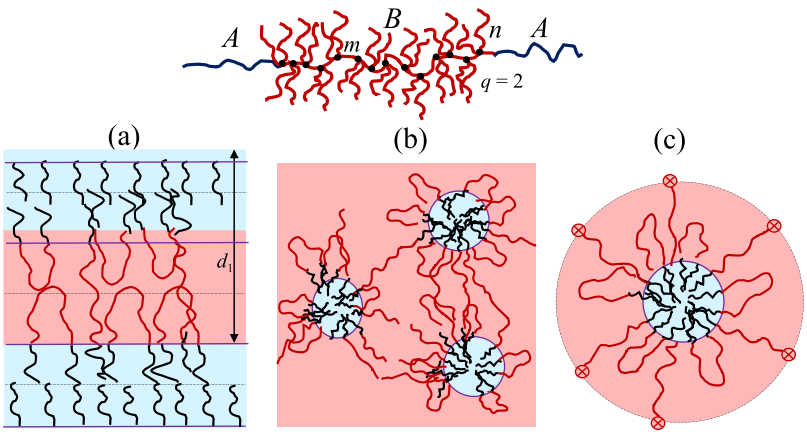

Figure 1. Schematic of the *ABA* block copolymer with a central comb-shaped block, and microphase-segregated structures in melts. Lamellar (a) and nonplanar (spherical, cylindrical) morphologies (b). Wigner−Seitz cell with half bridges attached to its boundary (c). Side chains of comb-shaped block are not shown.

comblike polymers with relatively loose grafts exhibit Gaussian statistics on all length scales in melts, the densely grafted side chains in bottlebrush polymers cause local stretching of the backbones. Using the asymptotic expressions for elasticity of branched polymers with long backbones, we examined three basic morphologies (spherical, cylindrical, and lamellar) of microphase-segregated melts in the strong segregation limit. Although the parabolic potential framework invokes the development of dead zones in convex brushes with nonplanar morphologies,[37−41] their presence was ignored in our previous study[36] due to conjecture that branching leads to a shrinkage of the dead zones[24,43] and thus that their effect on the equilibrium parameters of superstructures is minor.

In this paper, we quantitatively evaluate the effect of dead zones on the structural properties of microphase-segregated melts by implementing the two-layer model that was originally formulated for solvated cylindrical and spherical brushes of linear polymers.[41] We supplement the analytical model with the numerical Scheutjens−Fleer self-consistent field (SF-SCF) simulations of convex solvent-free brushes of comblike polymers with systematically varied lengths of side chains and spacers.

Using the two-layer model of dry brushes, we demonstrate that the effect of a dead zone could be noticeable in a spherical morphology, leading to smaller sizes of the domains and a mild shift in the binodal separating spherical and cylindrical superstructures to larger contents of a matrix-forming component.

Similarly to *AB* diblocks, triblock copolymers *ABA* with branched blocks give rise to spherical, cylindrical, and lamellar superstructures. More complex structures, e.g., a double gyroid,[42] are also possible. The major difference between microphase-segregated melts of *AB* and *ABA* block copolymers arises due to formation of *B* bridges by central blocks of *ABA* copolymers. In contrast to *B* loops returning to the same domains, *B* bridges connect neighboring domains giving rise to a physical network with architecture-dependent elasticity. While the presence of *B* bridges mildly affects the equilibrium dimensions of the domains and interdomain distances, the network elasticity is governed by both the fraction of bridges and the architecture of *B* blocks.

In our previous papers,[45,47] we analyzed how the grafting density and length of the side chains affect the equilibrium fraction of *B* bridges in lamellar mesophases of *ABA* block copolymers with a comb-shaped *B* block. We demonstrated that the equilibrium fraction of bridging chains in lamellae can be estimated from the equilibrium parameters of brushes formed by *B* subchains (i.e., loops cut in two equal parts) with the middle points of bridges pinched at the symmetry plain between grafting surfaces. This theoretical approach was checked and supported by the numerical Scheutjens−Fleer self-consistent field (SF-SCF) modeling. Note that while the analytical strong-stretching self-consistent field (SS-SCF) theory presumes a Gaussian elasticity of tethered macromolecules on all length scales and describes the set of chain conformations via "trajectories" (that is, the most probable positions of monomer units), numerical SF-SCF modeling accounts properly for conformational degrees of freedom irrespective of the extent of stretching of the brush-forming macromolecules, including the nonlinear elasticity regime. Using the SS-SCF and SF-SCF approaches, we demonstrated that comblike branching of *B* blocks leads to the structural organization of *B* layers resembling that of linear chains, that is, loops occupy the presurface regions in the apposing brushes, while the central part of the gap is filled with segments of bridges with associated side chains. However, the equilibrium fraction of bridges formed by comblike polymers noticeably decreases compared to linear chains with the same DP.

The goal of this study is 2-fold: (i) we first investigate how the fraction of bridging *B* chains connecting neighboring *A* domains depends on the morphology of the microphase-segregated state of the melt and on the architectural parameters of the *ABA* triblock copolymer, and (ii) we examine how the presence of dead zones affects the equilibrium parameters of microphase-segregated superstructures and the binodals separating ranges of thermodynamic stability of different morphologies.

The rest of the paper is organized as follows. In section 2, we consider solvent-free brushes formed by comblike macromolecules, introduce a two-layer model of dry convex brushes, and compare the analytical predictions to the results of numerical SF-SCF simulations. In section 3, the two-layer model was applied to describe the matrix in the microphase-segregated melt of the *ABA* copolymer. In section 4, we estimate the equilibrium fraction of the *B* bridges in microphase-segregated melts of *ABA* triblock copolymers versus the morphology of the *A* domains. In section 5, we examine the effect of dead zones on the equilibrium parameters

https://doi.org/10.1021/acs.macromol.2c00418
Macromolecules XXXX, XXX, XXX−XXX

of the superstructures and the binodals separating the spherical, cylindrical, and lamellar morphologies of copolymers with comb-shaped blocks. In section 6, we compare the theoretical predictions to experiments. In section 7 we formulate the conclusions.

2. BRUSH OF COMB-SHAPED MACROMOLECULES: MODEL AND SS-SCF FORMALISM

Consider a comb-shaped homopolymer comprised of $P \gg 1$ repeats each composed of the backbone spacer with a degree of polymerization (DP) m and $q \geq 1$ side chains with n monomer units each, linked to each junction on the backbone, see Figure 1. The backbone and side chains are assumed to be chemically identical and have monomer units with length l, volume v, and Kuhn segment $b > l$. If $q > 1$, the macromolecules are termed "barbwire" polymers. The backbone has DP $M = Pm$, while the total DP of the macromolecule is

$$N = P(m + qn) = M(1 + qn/m) \quad (1)$$

The macromolecules are tethered to an impermeable planar surface (AB interface) with area s per chain. The grafting density $\sigma = 1/s$ ensures strong overlap of individual macromolecules so that the backbones are extended in the direction normal to the grafting surface with a cutoff of polymer density profile (brush thickness) at distance $D = Nv/s$ from the surface.

Following the strong stretching self-consistent field (SS-SCF) approach formulated earlier,[36] the molecular potential $U(z)$ in a solvent-free brush exhibits a parabolic dependence on distance z from the grafting surface

$$\frac{U(z)}{k_B T} = \frac{3}{2lb}\kappa^2(D^2 - z^2) \quad (2)$$

with architecture-dependent topological coefficient κ. Equation 2 presumes the Gaussian (linear) elasticity of the tethered chains on all length scales. Crowding of the side chains near the branching points is not taken into account, which restricts the branching activity $q \simeq 1$. Other restrictions on the applicability of eq 2 are the possible appearance of dead zones depleted of the free ends of the backbones and vertical stratification for certain architectures of comb-shaped polymers. In these cases, eq 2 serves as an approximation to be checked by alternative scf methods, e.g., SF-SCF modeling.[46] The basic elements of the SF-SCF method are described in our preceding publication.[47]

The topological coefficient κ in eq 2 depends on the architectural parameters of the polymers with $q \geq 1$: DPs of the side chain (n), spacer (m), and backbone, $M = mP$. We demonstrated earlier[45] that κ exhibits different asymptotic dependences for polymers with short, $M \ll (mn/q)^{1/2}$, and long, $M \gg (mn/q)^{1/2}$, backbones. In this paper, we focus on comblike polymers with long backbones, $M \gg (mn/q)^{1/2}$, and use the corresponding asymptotic power law dependence for the topological coefficient κ

$$\kappa = \frac{\pi}{2N}\left(1 + \frac{qn}{m}\right)^{1/2} = \frac{\pi}{2M}\left(1 + \frac{nq}{m}\right)^{-1/2}, \quad M \gg (nm/q)^{1/2} \quad (3)$$

For linear chains with $q = 0$ and $N = M$, the topological coefficient $\kappa = \kappa_{lin} = \pi/2N$. To eliminate the molecular weight dependence of κ, we introduce the topological ratio

$$\eta = \frac{\kappa}{\kappa_{lin}} = \frac{2\kappa N}{\pi} \quad (4)$$

which is approximated as

$$\eta_{comblike} = \left(1 + \frac{qn}{m}\right)^{1/2} = (N/M)^{1/2} \quad (5)$$

for comblike polymers with $M \gg (mn/q)^{1/2}$ (locally unextended backbones). In conventional comblike polymers, $q = 1$.

The topological ratio η for bottlebrush (bb) polymers with locally extended backbones was also discussed earlier.[36] The onset of local backbone extension (i.e., the onset of the bottlebrush regime for comb-shaped polymer) is governed by dense packing of the backbone segment with associated side chains in volume V with radius $r_0 = (lbn)^{1/2}$ equal to the Gaussian size of side chain, that is

$$V = \frac{4\pi}{3}r_0^3 = \frac{4\pi}{3}(lbn)^{3/2} = vn\left(\frac{qn}{m_*} + 1\right) \approx v\frac{qn^2}{m_*} \quad (6)$$

to specify the threshold value m_* of spacer length as

$$m_* \approx \frac{3}{4\pi}\frac{v}{(lb)^{3/2}}qn^{1/2} \quad (7)$$

For comb-shaped polymers with $m \ll m_*$, the backbone is locally stretched and the topological ratio for such macromolecules is given by

$$\eta_{bottlebrush} = \alpha\frac{(lb)^{3/4}}{v^{1/2}}n^{1/4} \quad (8)$$

with the numerical coefficient $\alpha \simeq 1$. In this scenario, the topological coefficient $\kappa = \pi\eta_{bottlebrush}/(2N)$ in eq 2 should be renormalized according to eq 8.

Equations 8 and 5 indicate that the elastic free energy of comb-shaped polymers in a brush is dominated by stretching of their backbones while the side chains are weakly stretched and retain almost unperturbed Gaussian conformations.

2.1. Dead Zone in Dry Convex Brush: Two-Layer Model. In convex brushes of linear chains, the parabolic molecular potential leads to a negative number density of the free ends near the grafting surface, indicating the development of dead zones.[37] Dead zones emerge also for certain architectures of branched chains in a planar geometry.[48] Importantly, dead zones of any origin modify the parabolic shape of the molecular potential,[38,39] making its precise calculation challenging.

A simplified two-layer model accounting for dead zones in solvated convex brushes of linear chains[41] combined the power law decay in polymer density inside the dead zone with the planar-like distribution of chain segments in the brush peripheral region. Matching the polymer density profiles in the spherical (or cylindrical) dead zone and the planar-like peripheral layer, supplemented with length conservation of chain segments in both layers, relates the dead zone width, z_0, to the curvature of the grafting surface. It was demonstrated[41] and confirmed by more accurate calculations[39] that an inferior solvent strength leads to the increased relative extension of the dead zone, suggesting that dead zones could occupy a significant part of strongly curved solvent-free brushes of comb-shaped polymers.

https://doi.org/10.1021/acs.macromol.2c00418
Macromolecules XXXX, XXX, XXX−XXX

To evaluate the effect of dead zones on the properties of microphase-segregated melts of copolymers with comb-shaped blocks, we extend the original two-layer model[41] to dry, solvent-free brushes. In contrast to brushes swollen in solvent, matching of polymer volume fractions $\varphi(z)$ at $z = z_0$ occurs in a solvent-free brush automatically because $\varphi(z) = 1$ everywhere in both layers. In this case, z_0 is specified by matching the average elastic tensions at the boundary between the two layers. A detailed description of the two-layer model of dry brushes is presented in the SI. Here, we formulate the results relevant to further discussion.

In a convex solvent-free brush of comb-shaped polymers with DP N and volume υN, end tethered to a cylinder ($i = 2$) or sphere ($i = 3$) with radius R_i and area s_i per molecule (see Figure S1, SI), the brush thickness D_i is related to N and R_i as

$$\frac{iN\upsilon}{s_i R_i} = \left(1 + \frac{D_i}{R_i}\right)^i - 1 \tag{9}$$

The brush is divided into 2 layers: a dead zone with thickness z_0 near the surface and a peripheral layer with thickness $(D_i - z_0)$. The dead zone contains equally stretched segments of backbones, while the remaining backbone segments distribute free ends all over the planar-like peripheral layer. Introduction of the reduced variables

$$\omega_i = \frac{D_i}{R_i}; \quad y_i = \frac{z_0}{D_i} \tag{10}$$

and balance of the average elastic tensions at the boundary between the two layers ($z = z_0$) allow for equations for reduced width y_i of the dead zone in spherical ($i = 3$) and cylindrical ($i = 2$) geometries

$$y_3 = \frac{z_0}{D_3} = \left[\frac{1}{2}\left(\frac{\omega_3}{3} + 1 - \frac{\pi^2}{4}\right) + \sqrt{\frac{1}{4}\left(\frac{\omega_3}{3} + 1 - \frac{\pi^2}{4}\right)^2 + \left(\frac{\pi^2}{8} - \frac{1}{3}\right)\left(\frac{\omega_3^2}{3} + \omega_3 + 1 - \frac{\pi^2}{8}\right)}\right] \div \left[\omega_3\left(\frac{\pi^2}{8} - \frac{1}{3}\right)\right] \tag{11}$$

and

$$y_2 = \frac{z_0}{D_2} = \frac{2 + \omega_2 - \frac{\pi^2}{4}}{\omega_2\left(\frac{\pi^2}{4} - 1\right)} \tag{12}$$

The dead zone disappears (i.e., $y_i = 0$) if

$$\omega_i < \omega_{i,0} = \left(\frac{D_i}{R_i}\right)_0 = \begin{cases} -\frac{3}{2} + \sqrt{\frac{3\pi^2}{8} - \frac{3}{4}} \approx 0.218 & i = 3 \\ \frac{\pi^2}{4} - 2 \approx 0.467 & i = 2 \end{cases} \tag{13}$$

while its maximal relative width $y_i(\omega_i \to \infty)$ is given by

$$y_{i,\max} = \begin{cases} \frac{1}{\pi^2/4 - 1} \approx 0.681 & i = 2 \\ \frac{1/6 + \sqrt{1/36 + (\pi^2/8 - 1/3)/3}}{\pi^2/8 - 1/3} \approx 0.821 & i = 3 \end{cases} \tag{14}$$

Notably, eq 10 does not comprise the architectural parameters of comb-shaped polymers and is applicable to linear polymers as well.

In Figure 2, we present the reduced width of the dead zone, $y_i = z_0/D_i$, in spherical ($i = 3$) and cylindrical ($i = 2$) dry brushes (lines with symbols calculated according to eqs 11 and 12) as a function of the reduced curvature

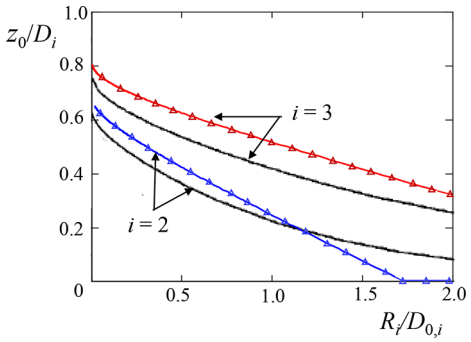

Figure 2. Relative extension of the curvature-induced dead zone, z_0/D_i, in a convex dry brush with thickness D_i, formed by linear chains with DP N, tethered to a convex surface with radius R_i and grafting area s_i per chain. $D_{0,i} = N\upsilon/s_i$ is the thickness of a planar brush with grafting area s_i per chain. Lines with symbols show z_0/D_i calculated with the two-layer model. Solid black curves are exact z_0/D_i according to ref 39.

$$\frac{R_i}{D_0} = \frac{R_i s_i}{N\upsilon} = \frac{i}{(1 + \omega_i)^i - 1} \tag{15}$$

Here, $D_0 = N\upsilon/s_i$ is the thickness of the planar solvent-free layer with grafting area s_i per chain. As it is seen in Figure 2, at strong curvature of a spherical surface, $R_3/D_0 \lesssim 2$, the ratio z_0/D_3 is rather close to the exact dependence[39] calculated for linear chains (shown by the upper solid lines in Figure 2). The correspondence between the approximate and the exact values of z_0/D_2 (lower solid line) at strong curvatures for a cylindrical geometry is reasonable as well. The maximal extensions of dead zones, $y_{3,\max} \approx 0.82$ and $y_{2,\max} \approx 0.68$, are close to the exact values, 0.71 and 0.63, respectively.[39] However, at weak curvatures ($\omega_i < \omega_{i,0}$), in contrast to the predicted exponential decay,[39] z_0 exactly equals zero in the two-layer model.

In the two-layer model, the elastic free energy F_{el} per chain in a convex brush of comb-shaped polymers comprises the elastic contributions due to the dead zone region ($F_{el,in}$) and the planar-like peripheral layer ($F_{el,out}$)

$$F_{el} = F_{el,in} + F_{el,out} \tag{16}$$

The elastic free energy F_{el} per molecule is calculated in the SI and is given by

https://doi.org/10.1021/acs.macromol.2c00418
Macromolecules XXXX, XXX, XXX−XXX

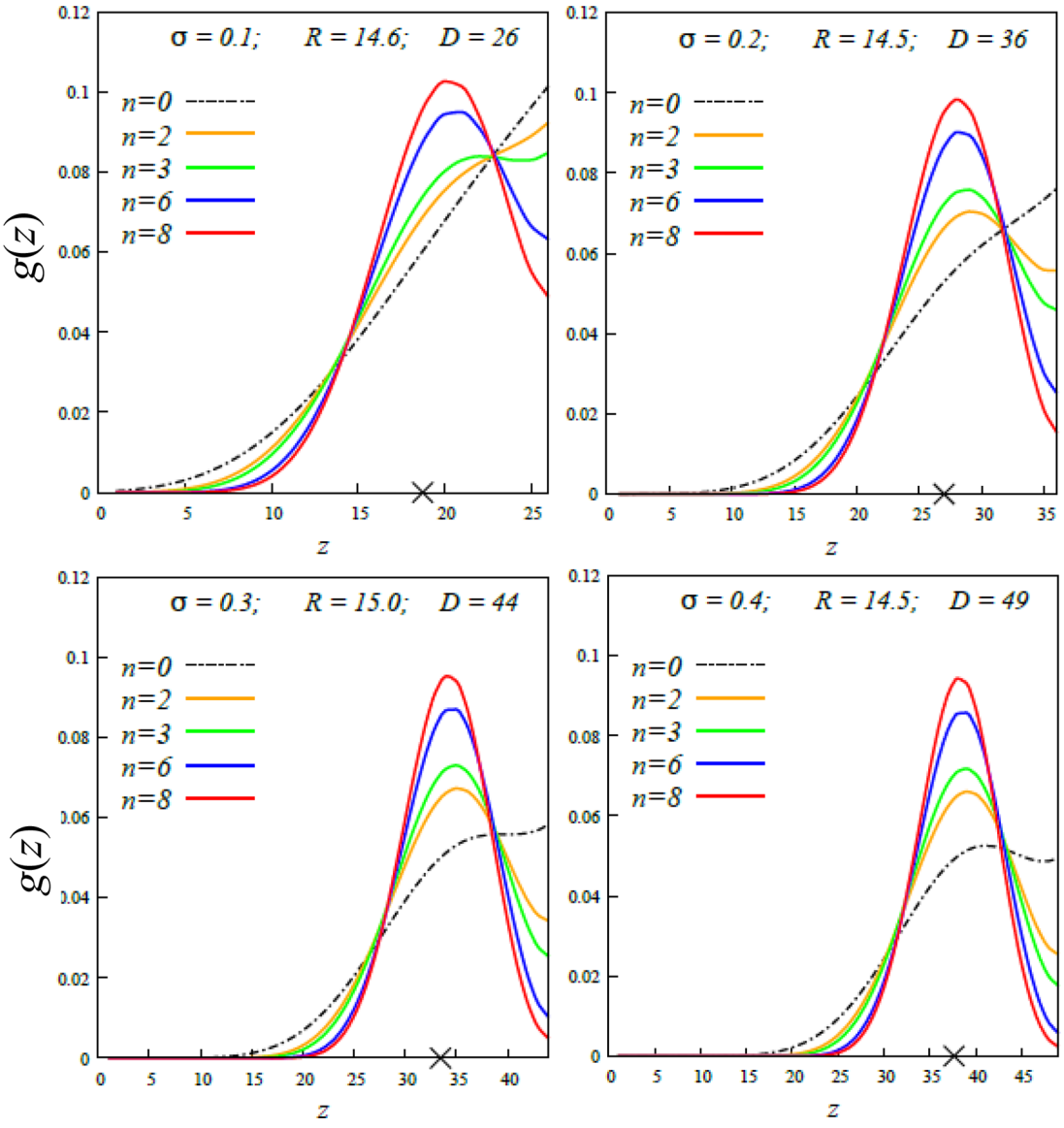

Figure 3. Fraction $g(z)$ of middle points in the spherical ($i = 3$) brush of loops formed by comblike polymer with fixed DP $N = M(1 + n/m) = 1000$ as a function of distance z from the surface. $m = 2$ values of other parameters (σ, R, D, n) are indicated in the plots. Theoretical thickness z_0 of the dead zone is indicated by cross on the z axis.

$$\frac{F_{el}}{k_B T} = \frac{\upsilon\eta^2}{lb}\frac{R_i}{s_i} \times \begin{cases} \frac{3}{2}\frac{y_i}{y_i + \omega_i} + \frac{27\pi^2}{8}\frac{\omega_3^3(1-y_3)^3[(1+y_3\omega_3)^2/3 + \omega_3(1+y_3\omega_3)(1-y_3)/2 + \omega_3^2(1-y_3)^2/5]}{[(1+\omega_3)^3 - (1+\omega_3 y_3)^3]^2} & i = 3 \\ \frac{3}{2}\ln\left(\frac{y_i + \omega_i}{y_i}\right) + \frac{3\pi^2}{2}\frac{\omega_2^3(1-y_2)^3[(1+y_2\omega_2)/3 + \omega_2(1-y_2)/4]}{[(1+\omega_2)^2 - (1+\omega_2 y_2)^2]^2} & i = 2 \end{cases} \quad (17)$$

2.2. SF-SCF Modeling of Convex Solvent-Free Brushes of Comb-Shaped Polymers. The details of the SF-SCF method have been described in detail in our previous publications.[45,47] Here, we present the scf data to merely confront the relevant analytical predictions. As before, we implement monomer size a as the unit length to make R, D, z_0, and grafting density $\sigma = s^{-1}$ dimensionless. More results of the numerical scf modeling and computer DPD simulations of microphase-segregated melts of comb-shaped polymers will be presented in a subsequent publication.

In Figure 3, we illustrate the development of a dead zone in a spherical ($i = 3$) solvent-free brush formed by loops of comb-shaped polymer. In the SF-SCF approach, a brush of loops with backbone DP M and grafting density σ is equivalent to the brush of linear chains with DP $M/2$ and grafting density 2σ. In Figure 3, the normalized to unity fraction $g(z)$ of middle points of the loops is presented as a function of distance z from the

https://doi.org/10.1021/acs.macromol.2c00418
Macromolecules XXXX, XXX, XXX−XXX

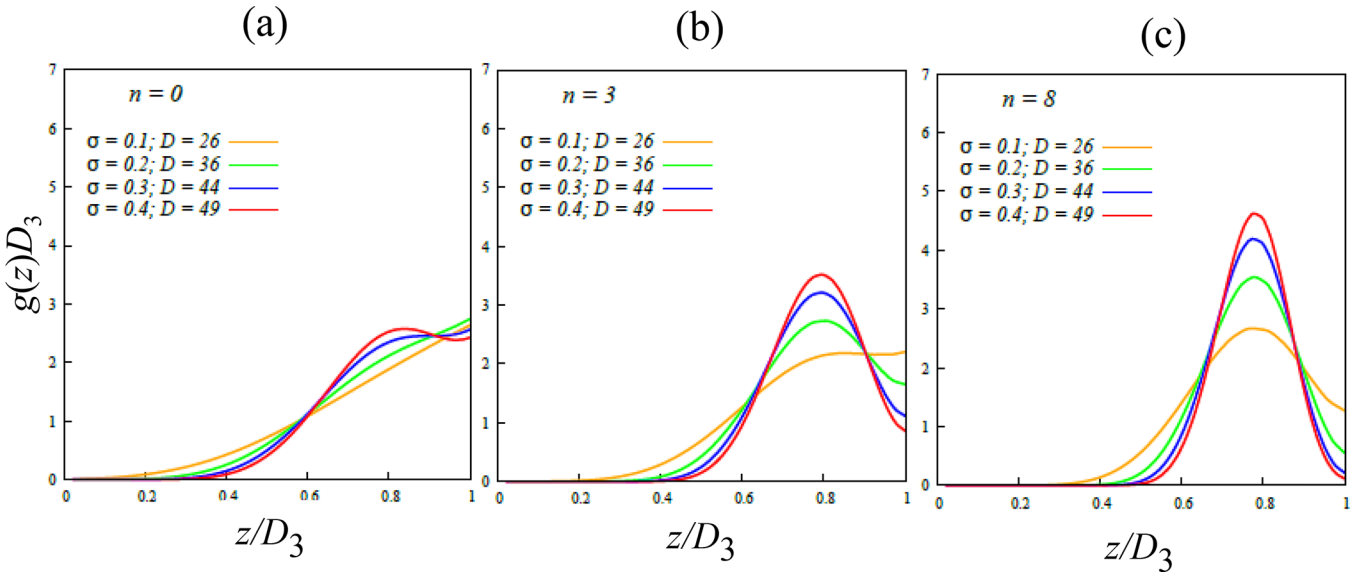

Figure 4. Normalized fraction $g(z)D_3$ of middle points in the brush of loops with fixed DP N = 1000 as a function of reduced distance z/D_3 from the surface of the spherical substrate with radius R_3 = 15 at different grafting densities σ. DP of the side chain n = 0 (a), 3 (b), and 8 (c).

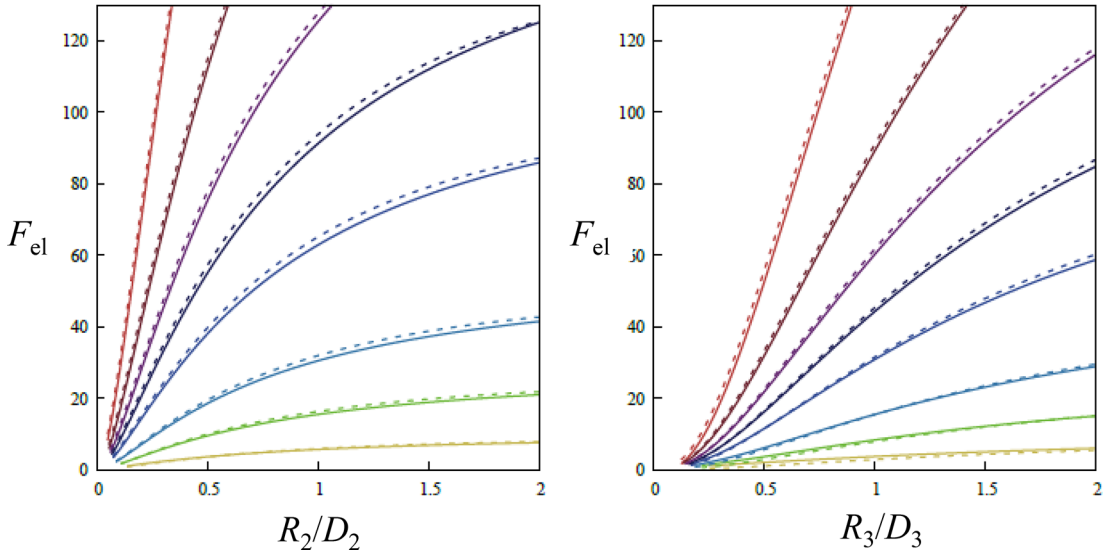

Figure 5. Free energy F_{el} per molecule (in k_BT units) in the cylindrical (i = 2, left) and spherical (i = 3, right) solvent-free brushes of loops formed by comblike polymer as a function of ratio R_i/D_i. Solid and dashed lines indicate scf data and analytical predictions calculated according to eq 20 (two-layer model), respectively. In both plots backbone DP M = 400, grafting density of loops σ = 0.1, m = 2, and n = 1, 3, 5, 8, 10, 12, 15, and 20 (curves indicated by different colors with n increasing from bottom to top).

surface at a fixed loop DP N = 1000, m = 2, $R_3 \approx 15$, and varied system parameters (indicated in the plots with subscript 3 omitted to avoid crowding). The theoretical thickness z_0 (eq 11) is indicated by a cross on the z axis. As it is seen in Figure 3, an increase in DP n of the side chains leads to the stretching of polymer backbones with DP $M = N(1 + n/m)$, the concomitant development of the maximum in $g(z)$ dependence, and the extension of the dead zone. A similar effect is invoked by the increase in the grafting density σ.

According to the two-layer model, the relative width of the outer (planar-like) sublayer depends only on the ratio R_i/D_i, and therefore, at a fixed surface radius, R_i = const, the distribution $g(z)$ of loop middle points (end points of the equivalent linear chains) depends only on the reduced distance z/D_i. Therefore, the two-layer model predicts a universal shape of the normalized distribution $g(z)D_i$ as a function of z/D_i with a maximum at the external boundary of the brush, z/D_i = 1. In Figure 4, we present $g(z)D_3$ as a function of z/D_3 in a spherical brush (i = 3) for comb-shaped polymer DP N = 1000 and varied lengths of the side chains, n = 0 (Figure 4a), n = 3 (Figure 4b), and n = 8 (Figure 4c). An increase in n and the concomitant decrease in $M = N/(1 + n/m)$ lead to localization of the normalized distribution $g(z)D_3$ around the same maximum (consistent with the analytical model). However, in contrast to the theoretical predictions, the position of the maximum in $g(z)D_3$ is shifted to smaller values of $z/D_3 \approx 0.8 < 1$. This shift could be rationalized as follows. In the case of comb-shaped polymers, the maximum in $g(z)D_3$ dependence is expected to shift to the left due to accommodation of the side chains that ensure dense packing of monomer units in the vicinity of the brush external boundary. This feature of comb-shaped polymers is not accounted for in the analytical model

https://doi.org/10.1021/acs.macromol.2c00418
Macromolecules XXXX, XXX, XXX−XXX

but is revealed in the scf numerical calculations. Simultaneously, an increase in n leads to stronger stretching of the backbones and the approach to their limiting extension. As a result, the maximum tends to shift in the opposite direction, i.e., closer to the brush external boundary. Due to these two counteracting factors, the location of the maximum could remain virtually unchanged upon increasing n but the scf width of the dead zone decreases compared to the theoretical z_0.

However, in spite of all of the discrepancies, the two-layer model is capable of adequately reproducing the behavior of the elastic free energy in convex brushes of comb-shaped polymers. Notably, the latter is of utmost important for the subsequent analysis of microphase segregation. In Figure 5, we present the elastic free energy F_{el} per molecule as a function of R_i/D_i in the cylindrical ($i = 2$) and spherical ($i = 3$) convex solvent-free brushes formed by loops with a fixed backbone DP $M = 400$. The solid lines indicate the scf numerical data, while the dashed lines are calculated according eq 17 (two-layer model). In both plots, the grafting density $\sigma = 0.1$, $m = 2$, and variations in n lead to the corresponding decrease in the backbone DP $M = N/(1 + n/m)$. As shown in Figure 5, the difference between the analytical and the numerical values of F_{el} is reasonably small which justifies the applicability of the two-layer model of the matrix in curved geometries.

3. MICROPHASE-SEGREGATED MELT OF *ABA* COPOLYMER: TWO-LAYER MODEL OF THE MATRIX

Let triblock copolymer *ABA* have DP N_A of blocks *A* and DP $2N_B$ of the central block *B*. The structural parameters v_j, l_j of the monomer units in the blocks and Kuhn segments b_j ($j = A, B$), specify the ratio[36]

$$\beta = \frac{l_A b_A v_B}{l_B b_B v_A} \tag{18}$$

Transformation of the *ABA* triblock copolymer in two diblock copolymer molecules *AB* with DP N_B of block *B* does not significantly change the equilibrium parameters of the *A* domains and *B* matrix in the strong segregation limit as the account of bridging invokes only minor correction to the free energy of the *B* block. For example, in a planar case ($i = 1$), the relative increase in the elastic free energy of the *B* block due to the presence of $X_{B,1}$ bridges per grafting area s_1 is estimated as $O(X_{B,1}^4) < 1\%$ at the maximal value of $X_{B,1} = 0.5$.[45] However, the development of dead zones in cylindrical and spherical morphologies might more strongly affect the elastic free energy of *B* blocks (as well as the sizes of *A* domains), and we adopt the two-layer model of convex brushes to describe the *B* matrix.

3.1. Elastic Free Energy of Comb-Shaped Block *B*.

If N and R_i introduced in the previous section are assimilated to DP N_B of block *B* in the *AB* diblock copolymer and radius of the *A* domain then the grafting area s_i per chain is related to the domain radius R_i as

$$s_i = iN_A v_A/R_i \tag{19}$$

and the total elastic free energy of the *B* block in the two-layer model is formulated as

$$\frac{F_{B,i}}{k_B T} = \frac{R_i^2}{l_A b_A N_A}\beta\eta_B^2 c_i(\omega_i, y_i) \tag{20}$$

with

$$c_3(\omega_3, y_3) = \begin{cases} \frac{1}{2}\frac{\omega_3 y_3}{1+\omega_3 y_3} + \frac{9\pi^2}{8}\omega_3^3(1-y_3)^3\frac{[(1+y_3\omega_3)^2/3 + \omega_3(1+y_3\omega_3)(1-y_3)/2 + \omega_3^2(1-y_3)^2/5]}{[(1+\omega_3)^3 - (1+\omega_3 y_3)^3]^2} & \omega_3 > \omega_{3,0} \\ \frac{9\pi^2}{8}\omega_3^3\frac{[1/3 + \omega_3/2 + \omega_3^2/5]}{[(1+\omega_3)^3 - 1]^2} & \omega_3 < \omega_{3,0} \end{cases} \tag{21}$$

and

$$c_2(\omega_2, y_2) = \begin{cases} \frac{3}{4}\ln(1+\omega_2 y_2) + \frac{3\pi^2}{4}\omega_2^3(1-y_2)^3\frac{[(1+y_2\omega_2)/3 + \omega_2(1-y_2)/4]}{[(1+\omega_2)^2 - (1+\omega_2 y_2)^2]^2} & \omega_2 > \omega_{2,0} \\ \frac{3\pi^2}{4}\omega_2^3\frac{[1/3 + \omega_2/4]}{[(1+\omega_2)^2 - 1]^2} & \omega_2 < \omega_{2,0} \end{cases} \tag{22}$$

Here, y_i is related to ω_i via eqs 11 and 12 and $\omega_{i,0}$ is specified in eq 13.

3.2. Free Energy per *AB* Block Copolymer Molecule.

Compared to the free energy of the diblock copolymer calculated in the SS-SCF approximation,[36] the free energy F_i per diblock *AB* copolymer in the two-layer model of the *B* matrix is reformulated as

$$\frac{F_i}{k_B T} = \frac{F_{A/B}}{k_B T} + \frac{F_{A,i}}{k_B T} + \frac{F_{B,i}}{k_B T} = \frac{i\gamma N_A v_A}{l_A^2 R_i} + \frac{R_i^2}{l_A b_A N_A}[b_i\eta_A^2 + \beta\eta_B^2 c_i(\omega_i, y_i)] \tag{23}$$

with the numerical coefficients

https://doi.org/10.1021/acs.macromol.2c00418
Macromolecules XXXX, XXX, XXX−XXX

$$b_i = \begin{cases} \pi^2/8, & i = 1 \\ \pi^2/16, & i = 2 \\ 3\pi^2/80, & i = 3 \end{cases} \quad (24)$$

and functions c_i specified by eqs 21 and 22. Here, the surface free energy $F_{A/B}$ and the elastic free energy $F_{A,i}$ of the domain-forming block A are not changed, while $F_{B,i}$ is modified to account for the dead zone.

Introduction of volumes $V_i = v_i N_i$ ($i = A, B$) and the ratio

$$x = \frac{V_B}{V_A} = \frac{v_B N_B}{v_A N_A} \quad (25)$$

relates x to ω_i as

$$\omega_i(x) = (1 + x)^{1/i} - 1 \quad (26)$$

and $y_i(\omega_i)$ and $c_i(\omega_i, y_i)$ in eqs 21 and 22 become functions of x as

$$y_i(\omega_i) \to y_i(x) \text{ and } c_i(\omega_i, y_i) = G_i(x) \quad (27)$$

At a small curvature of A domains ($\omega_i < \omega_{i,0}$, no dead zones in the B matrix), functions $G_i(x)$ coincide with the morphology-dependent functions $g_i(x)$ calculated in the parabolic potential framework[36]

$$G_i(x) = g_i(x) = \frac{\pi^2}{8}\begin{cases} x, & i = 1 \\ 6x^{-2}[(1+x)^{1/2} - 1]^4\left[\frac{1}{4} + \frac{1}{3}[(1+x)^{1/2} - 1]^{-1}\right], & i = 2 \\ 9x^{-2}[(1+x)^{1/3} - 1]^5\left[\frac{1}{5} + \frac{1}{2}[(1+x)^{1/3} - 1]^{-1} + \frac{1}{3}[(1+x)^{1/3} - 1]^{-2}\right], & i = 3 \end{cases} \quad (28)$$

while at a large curvature of A domains (i.e., at $\omega_i > \omega_{i,0}$) functions $G_i(x)$ are specified by eqs 26, 12, 11, 22,21, and 27. Notably, due to the absence of a curvature-induced dead zone in a planar morphology ($i = 1$), $G_1(x) \equiv g_1(x)$ at any x.

Minimization of F_i with respect to R_i in eq 23 gives

$$R_i = \left(\frac{i\gamma N_A^2 v_A b_A}{2\Phi_i(x) l_A}\right)^{1/3}; \; D_i = R_i[(1+x)^{1/i} - 1], \; i = 1, 2, 3 \quad (29)$$

and

$$\frac{F_i}{k_B T} = 3\left(\frac{i}{2}\right)^{2/3} N_A^{1/3} \Phi_i(x)^{1/3}\left(\frac{\gamma^{2/3} v_A^{2/3}}{l_A^{5/3} b_A^{1/3}}\right) \quad (30)$$

with

$$\Phi_i(x) = b_i \eta_A^2 + \beta \eta_B^2 G_i(x) \quad (31)$$

4. FRACTION OF BRIDGES IN MESOPHASES OF *ABA* BLOCK COPOLYMER

To estimate the equilibrium fraction $X_{B,i}$ of bridging comb-shaped B blocks in spherical ($i = 3$) and cylindrical ($i = 2$) morphologies, we use the previously implemented approach[47] to calculate fraction $X_{B,1}$ of the bridges in lamellae ($i = 1$). As we demonstrated earlier,[47] the equilibrium fraction of bridges formed by blocks B in a planar geometry ($i = 1$) is related to the elastic free energy $F_{B,1}(x)$ of B subchains (that is, loops cut into two equal parts) as

$$X_{B,1} \approx \frac{1}{1 + \left(1 + \frac{72}{\pi^4}\frac{F_{B,1}(x)}{k_B T}\right)^{1/3}} \quad (32)$$

Here, the elastic free energy per B subchain with DP N_B is specified as[36]

$$\frac{F_{B,1}(x)}{k_B T} = \frac{\pi^2}{8}\eta_B^2 \frac{D_1^2}{l_B b_B N_B} = \frac{\pi^2}{8} x \beta \eta_B^2 \frac{R_1^2}{l_A b_A N_A} = \frac{\pi^2}{8} x \beta \eta_B^2 N_A^{1/3} \frac{1}{2^{2/3}}\left(\frac{\gamma^{2/3} v_A^{2/3}}{l_A^{1/3} b_A^{5/3}}\right)\left(\frac{\pi^2}{8} + \frac{\pi^2}{8}\beta \eta_B^2 x\right)^{-2/3} \quad (33)$$

In contrast to lamellae, the free ends of B subchains in nonplanar morphologies are distributed only in the peripheral layers while the segments of B subchains in dead zones are stretched equally. Therefore, the difference in the elastic free energies of loops and bridges is associated merely with the difference in the free energies of segments of B subchains with free and pinched end points at the outer boundary of the peripheral layer (edge of the Wigner−Seitz cell).

In the two-layer model, the peripheral layers in spherical ($i = 3$) and cylindrical ($i = 2$) morphologies are assimilated to planar brushes of subchains with DP $N_{B,out}$

$$N_{B,out} = \left[\left(1 + \frac{D_i}{R_i}\right)^i - \left(1 + \frac{z_0}{R_i}\right)^i\right]\frac{s_i R_i}{i v} \quad (34)$$

tethered with area $s_{eff} = \frac{\pi^2}{8} s_i (1 + z_0/R_i)^{i-1}$. The elastic free energy $\Delta F_{B,i}(x)$ of chain segments in the peripheral layer with thickness $(D_i - z_0)$ is formulated (see SI) as

$$\frac{\Delta F_{B,i}(x)}{k_B T} = \frac{\pi^2}{8}\eta_B^2 \frac{(D_i - z_0)^2}{l_B b_B N_{B,out}} = \frac{\pi^2}{8}\eta_B^2 \frac{(D_i - z_0) v_B}{l_B b_B s_{eff}} = \eta_B^2 \frac{(D_i - z_0) v_B}{l_B b_B s_i (1 + z_0/R_i)^{i-1}} \quad (35)$$

Using eq 19 for surface area s_i per molecule in morphology i and eq 29 one finds

https://doi.org/10.1021/acs.macromol.2c00418
Macromolecules XXXX, XXX, XXX−XXX

$$\frac{\Delta F_{B,i}(x)}{k_B T} = \beta\eta_B^2\left(\frac{\gamma^{2/3}\upsilon_A^{2/3}}{b_A^{5/3}l_A^{1/3}}\right)N_A^{1/3}\begin{cases}\dfrac{\omega_2(1-y_2)}{2[1+\omega_2(x)y_2(x)]}\left[\dfrac{\pi^2}{16}+\beta n_B^2 G_2(x)\right]^{-2/3} & i=2\\ \dfrac{\omega_3(1-y_3)}{(12)^{1/3}[1+\omega_3(x)y_3(x)]^2}\left[\dfrac{3\pi^2}{80}+\beta n_B^2 G_3(x)\right]^{-2/3} & i=3\end{cases} \quad (36)$$

The equilibrium fraction $X_{B,i}$ of bridges in spherical ($i = 3$) and cylindrical ($i = 2$) morphologies of the *ABA* copolymer is then evaluated as

$$X_{B,i} \approx \frac{1}{1+\left(1+\frac{72}{\pi^4}\frac{\Delta F_{B,i}(x)}{k_B T}\right)^{1/3}},\ i=2,\ 3 \quad (37)$$

When the dead zone is absent (i.e., $z_0 = 0$), $\Delta F_{B,i}(x)$ reduces to the elastic free energy of *B* subchains in a planar layer with effective grafting area $s_{\text{eff}} = s_i(\pi^2/8)$ for $i = 2$, 3 and $s_{\text{eff}} = s_1$ for $i = 1$, calculated in the parabolic potential framework

$$\left(\frac{\Delta F_{B,i}(x)}{k_B T}\right)_{z_0=0} = \beta\eta_B^2 N_A^{1/3}\left(\frac{\gamma^{2/3}\upsilon_A^{2/3}}{b_A^{5/3}l_A^{1/3}}\right)\begin{cases}\dfrac{\pi^2}{2^{10/3}}x\left[\dfrac{\pi^2}{8}+\beta\eta_B^2 g_1(x)\right]^{-2/3} & i=1\\ \dfrac{1}{2}[(1+x)^{1/2}-1]\left[\dfrac{\pi^2}{16}+\beta n_B^2 g_2(x)\right]^{-2/3} & i=2\\ \dfrac{1}{(12)^{1/3}}[(1+x)^{1/3}-1]\left[\dfrac{3\pi^2}{80}+\beta n_B^2 g_3(x)\right]^{-2/3} & i=3\end{cases} \quad (38)$$

with $g_i(x)$ specified in eq 28.

Using eq 37 with $\Delta F_{B,i}(x)$ formulated in eq 36 for $z_0 > 0$ or eq 38 for $z_0 = 0$, one finds the equilibrium fraction $X_{B,i}$ of *B* bridges in planar, cylindrical, and spherical morphologies. The latter is an important factor in the mechanical properties of microphase-segregated melts. Notably, in all three morphologies, the two-layer model predicts a larger elastic free energy of bridges compared to loops, making $X_{B,i} < 0.5$.

In Figure 6, we present the equilibrium fraction $X_{B,i}$ of *B* bridges as a function of the volume fraction f_B of the *B* component for two values of N_A. Triangles indicate a spherical morphology and squares a cylindrical one. In the absence of a dead zone (to the left of f_B indicated by arrow), an increase in f_B leads to the decrease in fractions of bridges, $X_{B,2}$ and $X_{B,3}$. The onset of the dead zone in a spherical morphology (indicated by arrow), and further increase in the extension of the dead zone with increasing f_B leads to the increase in $X_{B,3}$ due to progressive accumulation of the free ends of *B* subchains closer to the boundaries of Wigner−Seitz cells. Therefore, according to the two-layer model, the equilibrium fraction $X_{B,i}$ of bridges in cylindrical ($i = 2$) and spherical ($i = 3$) geometries passes through a minimum upon the onset of a dead zone. Notably, a kink in $X_{B,i}$ at the onset of a dead zone is related to approximations imposed in the two-layer model to find z_0. We anticipate that rigorously calculated z_0 would smooth the kink while preserving the minimum in $X_{B,i}(f_B)$ dependence.

In Figure 7, the equilibrium fraction of bridges $X_{B,i}$ is presented as a function of f_B for triblock copolymers with $N_A = 100$ and different topological ratios for *B* blocks, $\eta_B = 2$ (Figure 7a) and $\eta_B = 5$ (Figure 7b). Transitions between morphologies are accompanied by jumps in $X_{B,i}$. As shown in Figures 6 and 7, according to the two-layer model, fraction $X_{B,3}$ of bridges approaches 0.5 at $f_B \to 1$ and weakly depends of η_B.

The predicted trends in the behavior of $X_{B,3}$ are consistent with MD simulations[50,51] of self-assembling *ABA* networks with spherical domains. Both the simulations and the two-layer model predict the decrease in $X_{B,3}$ upon increasing N_A and the increase in fraction $X_{B,3}$ of bridges upon increasing $f_B \approx N_B = M_B(1 + n_B/m_B)$. However, MD simulations of dry networks[50] revealed the values of $X_{B,3} > 0.5$, pointing at a smaller elastic free energy of bridges compared to loops, while the two-layer model predicts $X_{B,3} < 0.5$. The discrepancy could arise due to relatively short copolymer blocks in MD simulations.[50] The short backbones in microphase-segregated structures are more stretched than long ones, decreasing the difference between the elastic free energies of loops and bridges. The filling constraints ($\varphi_B = 1$ everywhere in *B* matrix) and penalties due to backward turns in the stretched loops might favor a bridging conformation of the *B* block, leading to $X_{B,3} > 0.5$. However, the MD simulations of self-assembling *ABA* networks with swollen in solvent *B* blocks[51] indicated $X_{B,3} < 0.5$ and were also consistent with the predicted increase in fraction $X_{B,3}$ of bridges upon increasing f_B. f6f7

5. BINODALS IN THE TWO-LAYER MODEL OF THE *B* MATRIX

In the cylindrical geometry ($i = 2$), the dead zone in the *B* layer emerges at $x = x_{0,2} \approx 1.153$ (or equivalently at $f_B = f_{2,0} \approx 0.536$), while for spheres ($i = 3$), the onset of the dead zone is shifted to $x_{0,3} \approx 0.806$ (or $f_B = f_{0,3} \approx 0.446$). Therefore, depending on the ratio $x = V_B/V_A$, equations for binodals Y_{LC} and Y_{CS} (specified, respectively, as $F_1 = F_2$ and $F_2 = F_3$) are modified in the two-layer model as

https://doi.org/10.1021/acs.macromol.2c00418
Macromolecules XXXX, XXX, XXX−XXX

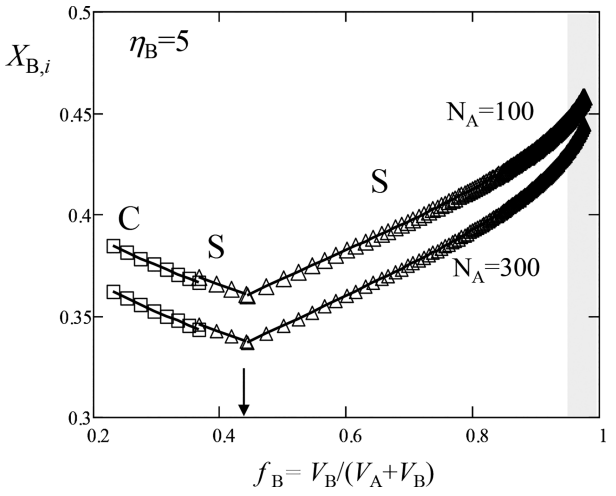

Figure 6. Equilibrium fraction $X_{B,i}$ of B bridges in cylindrical (C) and spherical (S) morphologies formed by *ABA* triblock copolymer with linear A and comb-shaped B blocks as a function of volume fraction f_B of the B component for two values of N_A (indicated near the curves). $\eta_B = 5$, $\eta_A = 1$. Squares correspond to cylinders ($i = 2$) and triangles to spheres ($i = 3$). Onset of dead zone occurs in spherical morphology at $f_B = f_{0,3} = 0.446$ shown by arrow. In shaded area, chain segments in the peripheral layer loose stretching.

$$Y_{LC} = \beta^{1/2}\left(\frac{\eta_B}{\eta_A}\right)_{LC} = \sqrt{4b_2 - b_1}\cdot\begin{cases} 1/\sqrt{g_1(x) - 4g_2(x)} & x < x_{0,2} = 1.153 \\ 1/\sqrt{g_1(x) - 4G_2(x)} & x > x_{0,2} \end{cases} \quad (39)$$

$$Y_{CS} = \beta^{1/2}\left(\frac{\eta_B}{\eta_A}\right)_{CS} = \sqrt{9b_3 - 4b_2}\cdot\begin{cases} 1/\sqrt{4g_2(x) - 9g_3(x)} & x < x_{0,3} = 0.806 \\ 1/\sqrt{4g_2(x) - 9G_3(x)} & x_{0,2} > x > x_{0,3} \\ 1/\sqrt{4G_2(x) - 9G_3(x)} & x > x_{0,2} \end{cases} \quad (40)$$

In Figure 8, we present binodals calculated with the SS-SCF parabolic potential framework ($Y_{LC,par}$ and $Y_{CS,par}$, presented earlier in ref 36) and binodals Y'_{LC} and Y'_{CS} calculated for fixed end points of B backbones in lamellar ($i = 1$), cylindrical ($i = 2$), and spherical ($i = 3$) morphologies. The latter correspond to $y_i = 1$ in eq 20 and are indicated by filled triangles. Below we refer to the model with end points of backbones fixed at external boundaries of Wigner–Zeitz cells as an "extended Semenov's model" in analogy with his original model of spherical and cylindrical matrices in microphase-segregated block copolymers with linear blocks.[37] If the free ends of backbones spread in lamellar layers then the corresponding L–C binodal, Y''_{LC}, is shown by the line with unfilled circles. As shown in Figure 13, for linear B blocks ($\eta_B = \eta_A = 1$) and $\beta = 1$, the transition compositions f_{LC} and f_{CS} (corresponding to respective intersections of $Y_{LC,par}$, $Y_{CS,par}$ and Y''_{LC}, Y'_{CS} with the x axis) are quite close in the SS-SCF framework ($f_{LC} \approx 0.704$, $f_{CS} \approx 0.886$) and Semenov's model[37] ($f_{LC} \approx 0.717$, $f_{CS} \approx 0.874$). The latter model allows for distribution of the free end points of linear B blocks in lamellae and fixed end points of B blocks in cylindrical and spherical morphologies. In the case of fixed end points of linear B blocks in lamellae, f_{LC} decreases to $f_{LC} \approx 0.615$.

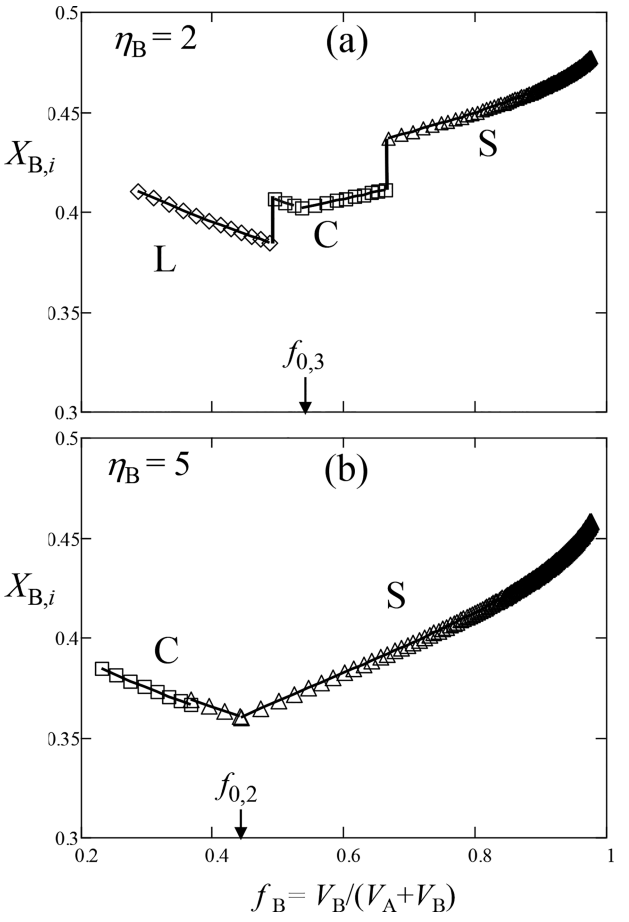

Figure 7. Equilibrium fraction $X_{B,i}$ of B bridges in lamellar (L), cylindrical (C), and spherical (S) morphologies formed by triblock *ABA* copolymer with linear A and comblike B blocks as a function of volume fraction f_B of the B component for $\eta_B = 2$ (a) and $\eta_B = 5$ (b), $\eta_A = 1$. Diamonds correspond to lamellae ($i = 1$), squares to cylinders ($i = 2$), and triangles to spheres ($i = 3$). Onsets of dead zone $f_B = f_{0,2} = 0.54$ for $i = 2$ and $f_B = f_{0,3} = 0.45$ for $i = 3$ are shown by arrows. Transitions between morphologies are accompanied by jumps in $X_{B,i}$.

Branching of B blocks and an increase in η_B lead to progressive deviations of Y'_{LC}, Y''_{LC} from $Y_{LC,par}$ and Y'_{CS} from $Y_{CS,par}$. If the end points of the B backbones in the lamellar morphology remain free, the L–C binodal Y''_{LC} intersects Y'_{CS} at $\eta_B \approx 3$, indicating destabilization of the cylindrical morphology. This discrepancy is directly related to different approximations for end-point distributions of backbones in planar ($i = 1$) and nonplanar ($i = 2, 3$) morphologies. If the end points of backbones in the B layers are fixed at the outer boundaries of the Wigner–Seitz cells in all of the geometries (including lamellae) then the L–C binodal Y'_{LC} is located below $Y_{LC,par}$, providing the corridor of stability for the cylindrical morphology.

Clearly, the L–C binodal Y_{LC} calculated with the two-layer model of the B matrix must be located between $Y_{LC,par}$ (no dead zone, $z_0 = 0$) and Y''_{LC} (dead zone extends to the whole B layer, $z_0 = D_2$), being closer to Y''_{LC} at $f_B \lesssim f_{CL} \approx 0.717$ and approaching $Y_{LC,par}$ upon decreasing f_B (and concomitant

https://doi.org/10.1021/acs.macromol.2c00418
Macromolecules XXXX, XXX, XXX–XXX

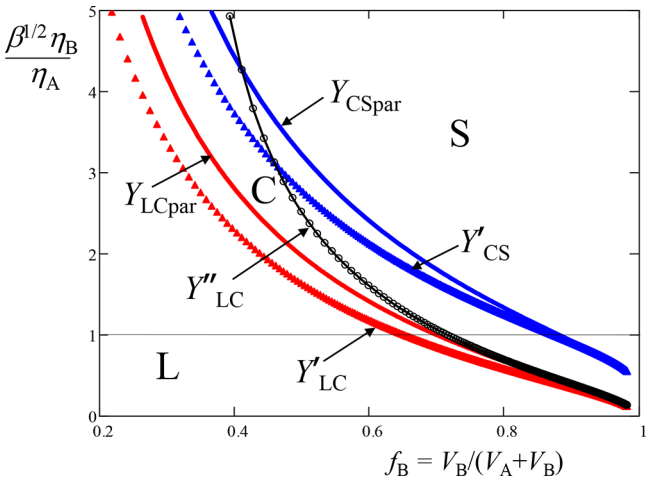

Figure 8. Binodals $Y = \beta^{1/2}\eta_B/\eta_A$ separating spherical (S), cylindrical (C), and lamellar (L) morphologies as a function of $f_B = V_B/(V_A + V_B)$, calculated with a parabolic potential framework ($Y_{CS,par}$, $Y_{LC,par}$, shown by solid lines) and an extended Semenov model (Y'_{CS}, Y'_{LC}, shown by triangles). Y''_{LC} (line with unfilled circles) indicates binodal between lamellae with unrestricted free ends of B backbones and cylinders with ends of B backbones fixed at the outer boundary of the Wigner−Zeit cell. Intersections of binodals with the black line $\beta^{1/2}\eta_B/\eta_A = 1$ correspond to morphological transitions in topologically symmetrical (including linear−linear) block copolymers. Binodals for inverted structures (B domains in the A matrix) are not shown.

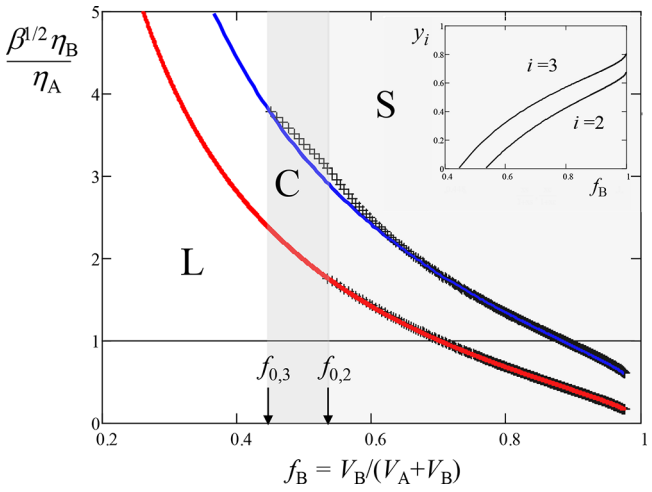

Figure 9. Binodals separating spherical (S), cylindrical (C), and lamellar (L) morphologies calculated with a parabolic potential framework (solid lines) and with a two-layer model (crosses). Arrows indicate block copolymer compositions, $f_{0,3} = 0.446$ and $f_{0,2} = 0.536$ corresponding to the onset of dead zone formation in the two-layer model. At $f_B < f_{0,3}$ (white area), no dead zones in the B layers, at $f_{0,3} < f_B < f_{0,2}$, dead zones emerge only in spherical morphology (dark gray area), while at $f_B > f_{0,2}$, dead zones emerge in both cylindrical and spherical morphologies (light gray area). (Inset) Relative width $y_i = z_0/D_i$ of dead zones in spherical ($i = 3$) and cylindrical ($i = 2$) B layers. Intersections of binodals with the black line $\beta^{1/2}\eta_B/\eta_A = 1$ correspond to morphological transitions in topologically symmetrical (including linear−linear) block copolymers. Binodals for inverted structures (B domains in A matrix) are not shown.

decrease in z_0), that is, Y_{LC} should shift to the right of $Y_{LC,par}$ due to the presence of a dead zone. A similar shift to the right of $Y_{CS,par}$ is expected for C−S binodal Y_{CS} due to larger extension of the dead zone in the spherical morphology.

f9 In Figure 9, we present L−C and C−S binodals as a function of volume fraction $f_B = V_B/(V_A + V_B)$ of the B component, calculated with the two-layer model of the B matrix (eqs 39 and 40). Solid lines indicate binodals $Y_{LC,par}$ and $Y_{CS,par}$ obtained in the parabolic potential framework[36] (first lines in eqs 39 and 40, extended to all x). Symbols (crosses) indicate sections of binodals Y_{LC} and Y_{CS} corrected for dead zones, i.e., emerging at $f_B > f_{0,2} \approx 0.536$ for $i = 2$ (the second line in eq 39), and $f_B > f_{0,3} \approx 0.446$ for $i = 3$ (the second and third lines in eq 40). The values of $f_{0,2}$ and $f_{0,3}$ do not depend on the modes of branching of the B blocks (i.e., do not depend on η_B) and are shown by arrows. Clearly, deviations of corrected binodals from $Y_{LC,par}$ and $Y_{CS,par}$ are small (numerical estimates are presented in the SI). Although the two-layer model ignores the presence of a curvature-induced dead zone at $f_B < f_{0,2}$ and $f_B < f_{0,3}$, we believe that corrections to $Y_{LC,par}$ and $Y_{CS,par}$ remain small there as well due to an exponential decrease[39] in the width of the dead zone at small curvatures.

f10f11 In Figures 10 and 11, we present ratios $r_i(\eta_B, x) = R_{i,par}/R_i$ of the domain radius $R_{i,par}$ calculated using the parabolic potential framework and R_i calculated with the two-layer model of the B matrix for spherical ($i = 3$) and cylindrical ($i = 2$) morphologies, respectively, as a function of $f_B = x/(1 + x) = v_B N_B/(v_A N_A + v_B N_B)$. As shown in Figure 11, the two-layer model predicts almost no affect of dead zone on r_2 in the range of stability of cylindrical domains: $R_{2,par}$ exceeds R_2 by less than 1%. The effect of dead zones on R_3 is stronger. An increase in ratio $r_3 = R_{3,par}/R_3$ in the range of $f_B < 0.9$ in Figure 10 indicates the decrease in R_3 by less than ~2%. At larger $f_B >$ 0.9, the radius of the A domain R_3 declines sharply. However, progressive branching of B blocks (i.e., an increase in η_B) shifts

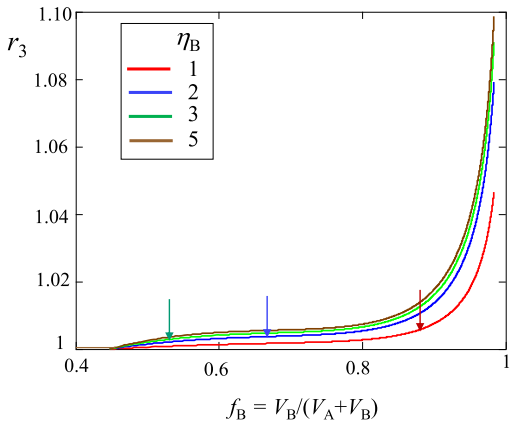

Figure 10. Ratio $r_3 = R_{3,par}/R_3$ of spherical domain radii calculated with a parabolic potential ($R_{3,par}$) and two-layer model (R_3) as a function of diblock copolymer composition f_B and topological ratio η_B of matrix block $\eta_A = 1$, $\beta = 1$. Onsets of thermodynamic stability for spherical morphology are indicated by arrows: $f_B = 0.525$, 0.666, and 0.883 for $\eta_B = 3$, 2, and 1, respectively. For $\eta_B = 5$, arrow at $f_B = 0.366$ is not shown. To the right of each arrow spherical domains are stable and to the left metastable.

the onset of stability of spherical domains (indicated by arrows in Figure 10) to smaller values of f_B, providing a wider interval of stability for the spherical morphology. Therefore, the difference between $R_{3,par}$ and R_3 in a wide range of $f_B \lesssim 0.97$ is predicted to be less than 10%, supporting the application of the SS-SCF framework to calculate the equilibrium parameters of the spherical and cylindrical domains.

https://doi.org/10.1021/acs.macromol.2c00418
Macromolecules XXXX, XXX, XXX−XXX

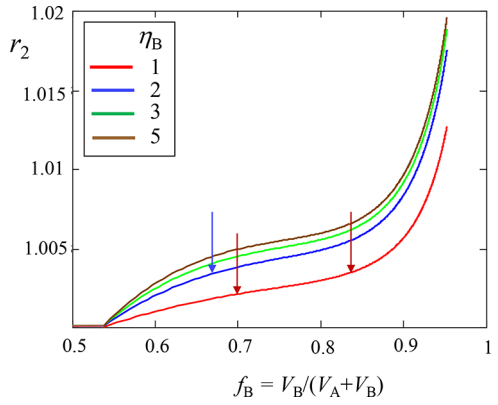

Figure 11. Ratio $r_2 = R_{2,par}/R_2$ of cylindrical domain radii calculated with a parabolic potential ($R_{2,par}$) and two-layer model (R_2) as a function of diblock copolymer composition f_B and topological ratio η_B of matrix block $\eta_A = 1$, $\beta = 1$. Cylinders are thermodynamically stable between the two arrows located at $f_B = 0.701$ and 0.883 for $\eta_B = 1$ and to the left of the arrow at $f_B = 0.666$ for $\eta_B = 2$. No thermodynamically stable cylinders at $f_B > 0.5$ for $\eta_B = 3$ and $\eta_B = 5$.

6. COMPARISON TO EXPERIMENTS

In our previous publication[36] we checked the predicted exponent 2/3 in the molecular mass dependence of the domain size, $R_i(N_A)$, for sets of chemically different *AB* and *ABA* copolymers with bottlebrush *B* blocks. Here, we perform a more refined comparison between the theoretical predictions and the experimental data.

Microphase-segregated triblock *ABA* copolymers, PMMA−PDMS−PMMA, with bottlebrush PDMS and linear PMMA blocks were experimentally examined in the series of papers by Sheiko et al.[16,19,49] These copolymers had high volume fractions f_B of PDMS (*B* component) and gave rise to spherical PMMA domains in the PDMS matrix upon evaporation of nonselective solvent toluene. The data for series of samples with $m_B = 1$ and $n_B = 14$ and 70 are collected in Table S1 in the SI in the upper and lower panels, respectively.

In localizing these copolymers in the morphological diagram of states[36] we treated the PDMS block as a bottlebrush polymer with $q_B = 1$ and $\beta \approx 1.26$ for the PDMS/PMMA pair, that is, the PDMS block was envisioned as a linear chain of N_0 impermeable superblobs with radius $r_0 = (l_B b_B n_B)^{1/2}$ and effective Kuhn length $\simeq r_0$.[52] While the backbone in each superblob is strongly elongated, the bottlebrush conformations in the melts remain Gaussian on larger scales with the backbone average end-to-end distance $R_0 \simeq r_0 N_0^{1/2}$. On the basis of this model, the topological coefficient η_B for the PDMS block with $n_B = 14$ was estimated via eq 8 with the numerical coefficient $\alpha_B = 0.5$ to give $\eta_B \approx 1.13$ and position $\beta^{1/2}\eta_B \approx 1.27$ for this PMMA−PDMS-PMMA series in the morphological diagram.[36] Notably, α_B served as an adjustable parameter to match the theoretical value of the C−S binodal to the experimental volume fraction $f_B \approx 0.82$, corresponding to first detection of PMMA domains with nonspherical geometry.

It should be emphasized, however, that superblob impermeability arises due to conformational losses associated with extra stretching of the side chains upon superblob interpenetration. Therefore, the concept of an impermeable superblob becomes progressively more accurate for barbwire polymers with $m_B = 1$ and increasing $q_B > 1$, i.e., with side chains stretching beyond the Gaussian size, r_0. The superblobs in conventional bottlebrushes with $q_B = 1$ still experience interpenetration, and estimation of m_{B^*} according to eq 7 for the PDMS parameters ($\upsilon_B = 136$ Å^3, $l_B = 2.5$ Å, $b_A = 13$ Å) gives $m_{B^*} \simeq 0.67$ for $n_B = 14$ and $m_{B^*} \approx 1.51$ for $n_B = 70$. Therefore, according to eq 7, experimental PDMS blocks with $m_{B^*} \simeq 1$ are found at the crossover between comblike and bottlebrush regimes.

An alternative option in analyzing the experimental data is to use η_B corresponding to the scale-independent Gaussian elasticity of the backbone in the *B* block. In this scenario, $\eta_B \approx (1 + n_B/m_B)^{1/2}$ for comb-shaped blocks with long backbones yielding $\eta_B \approx 3.87$ for $m_B = 1$ and 14. Below, we use both expressions for η_B (eqs 5 and 8) in confronting the theoretical predictions to the experimental data. Due to large content of PDMS in the PMMA−PDMS-PMMA block copolymers ($f_B > 0.8$), we apply the two-layer model of the *B* matrix to calculate the equilibrium radius R_3 of the *A* domain (eqs 29 and 31 for $i = 3$).

The structural parameters of the microphase-segregated melt of PMMA−PDMS−PMMA (*ABA*) copolymer with a spherical morphology[16,19,49] are collected in Table S1 in the SI. The experimentally measured[19] radius R_3^{exp}(Å) of the PMMA *A* domains in a series of samples with $n_B = 14$ (upper panel in Table S1) is presented in Figure 12 as a function of DP N_A of

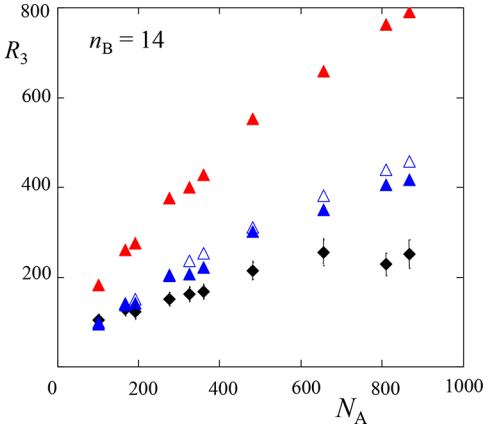

Figure 12. Radii R_3(Å) of the *A* domain in a microphase-segregated melt of triblock copolymer *ABA* with molecular brush *B* block as a function of DP N_A of linear block *A*. In the *B* block, $n_B = 14$, $m_B = 1$, $\beta = 1.26$. Experimental R_3 for PMMA−PDMS−PMMA copolymers[16,49] are indicated by diamonds with error bars. Red filled triangles indicate theoretically calculated R_3 (eq 29) for the *B* block treated as a bottlebrush with $\eta_B = 1.13$; blue filled triangles correspond to treatment of the *B* block as comblike with $\eta_B = (1 + n_B/m_B)^{1/2} = 15^{1/2}$ in the two-layer model. Unfilled triangles indicate theoretical values of R_3 in the SS-SCF parabolic potential framework.

the PMMA block (black diamonds with error bars). Filled triangles indicate R_3^{theor} calculated according to eqs 29 and 31 with $\eta_B = 1.13$ and 3.87, respectively, for values of parameters $\gamma = 0.37$,[44] $\beta = 1.26$, $\upsilon_A = 141$ Å^3, $l_A = 2.5$ Å, and $b_A = 17$ Å. Unfilled blue triangles indicate R_3^{theor} calculated in the parabolic SS-SCF approximation (eqs 29and 31 with $G_3 = g_3$). As shown in Figure 12, modeling the PDMS block *B* as a bottlebrush polymer, i.e., as a linear chain of impermeable

https://doi.org/10.1021/acs.macromol.2c00418
Macromolecules XXXX, XXX, XXX−XXX

superblobs with η_B = 1.13 (red filled triangles), strongly overestimates the domain radius R_3^{exp}, while the scale-independent Gaussian backbone elasticity (η_B = 3.87, blue filled triangles) leads to a better correspondence with the experimental data. The difference between filled and unfilled blue triangles (i.e., between predictions of the SS-SCF model and the two-layer model) is minor.

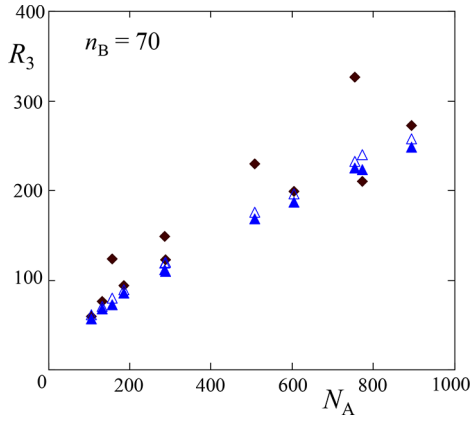

Figure 13. Radii R_3(Å) of *A* domains in a microphase-segregated melt of triblock copolymer *ABA* with a comb-shaped *B* block with n_B = 70 as a function of DP N_A of a linear block. Experimental radii $R_{3,\,exp}$ are shown by diamonds. Theoretical values of R_3 calculated with the SS-SCF parabolic potential framework and the extended Semenov's model are indicated by filled and unfilled triangles, respectively. *B* blocks were treated as comblike polymers with $\eta_B = (1 + n_B/m_B)^{1/2}$ and m_B = 1.

In Figure 13, we compare R_3^{exp} for PMMA–PDMS-PMMA samples with n_B = 70 (diamonds) to the theoretically predicted R_3^{theor} calculated according to eqs 29 and 31 with $\eta_B = (1 + 70)^{1/2} \approx 8.43$ (triangles). Similarly to the series with n_B = 14 (Figure 12), modeling the *B* block as a linear chain of impermeable superblobs considerably overestimates R_3^{exp} (not shown in Figure 13). Notably, in both series, the backbones in the *B* blocks are strongly elongated, even approaching the backbone contour length in some samples with n_B = 70. However, the two-layer model partially compensates for the nonlinear elasticity of the backbones via overestimated elongation near the surfaces of the *A* domains (see SI).

In Figure 14, we present the normalized domain radius $R_{norm} = \left(\frac{2\Phi_3(x)l_A}{3\gamma v_A b_A}\right)^{1/3} R_3^{exp}$ as a function of N_A. The data for samples with stronger stretched backbones (n_B = 70, unfilled symbols) and less stretched backbones (n_B = 14, filled symbols) fall predominantly above and below the theoretical asymptote, $R_{norm}^{theor} = N_A^{2/3}$ (shown by the straight line with slope 2/3). One would expect that samples with stronger elongated backbones (i.e., series with n_B = 70) would deviate below R_{norm}^{theor} due to smaller values of the equilibrium domain radius. In contrast, the majority of samples with n_B = 70 demonstrate a larger domain radius than predicted by the two-layer model. The deviations of the data for n_B = 70 above the theoretical asymptote R_{norm}^{theor} correlate with the shift from a comblike to a bottlebrush regime for the *B* block upon

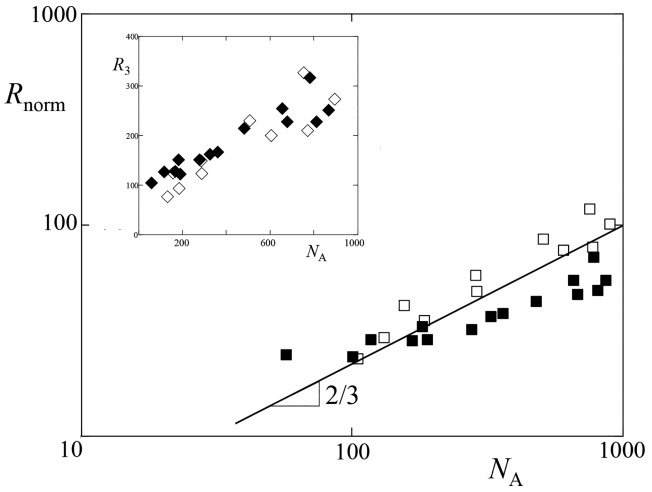

Figure 14. Normalized radius $R_{norm} = R_3^{(exp)}[(2l_A\Phi_3)/(3\gamma v_A b_A)]^{1/3}$ of the *A* domain in a microphase-segregated melt of triblock copolymer *ABA* with molecular brush *B* block as a function of DP N_A of the linear block. Topological ratio for *B* blocks was calculated as $\eta_B = (1 + n_B/m_B)^{1/2}$ with m_B = 1. Filled and unfilled symbols correspond to n_B = 14 and 70, respectively. Straight line is the theoretically predicted asymptote, $R_{norm} = N_A^{2/3}$. (Inset) Raw data for $R_3^{(exp)}$ (error bars are not shown).

increasing n_B. The discrepancy could also arise due to a lack of equilibration of the self-assembling networks of the *ABA* block copolymers. At the same time, the relative deviations from the asymptotic dependence $R_{norm}^{theor} = N_A^{2/3}$ are moderate in both cases, indicating that the two-layer model with a scale-independent elasticity of *B* blocks could still describe the structure of microphase-segregated *ABA* melts with reasonable accuracy.

To illustrate that implementation of the scale-independent Gaussian elasticity for backbones allows for better agreement with the experiments, we present here also the data for PS–PDMS (*AB*) diblock copolymers with comb-shaped blocks[13] that self-assemble in lamellar structures (i = 1). All of the selected samples (listed in Table S2 in SI) have one side chain per monomer unit of norbornene backbone in each block, and both backbones have DP $M_i > n_i^{1/2}$. The latter condition allows us to use eq 5, which is asymptotically valid in the limit of $M_i \gg n_i^{1/2}$. Equation 5 for the topological coefficient with q_i = 1 and m_i = 1 is applicable to both blocks if they are treated as comblike homopolymers with equal sizes of monomer units in the backbone and side chain.[45] If, however, both blocks are treated as bottlebrushes, their topological ratios are calculated as $\eta_i = \alpha_i(l_i b_i)^{3/4} v_i^{-1/2} n_i^{1/4}$ (eq 8) with numerical coefficients $\alpha_i \simeq 1$. Evaluation of m_* (eq 7) for samples listed in Table S2 indicated that the PS blocks (with m_* = 0.76 for n_A = 29, and m_* = 1.14 for n_A = 48) as well as the PDMS block (with m_* = 1.41 for n_B = 65) were at the crossover between the comblike and the bottlebrush regimes, and we used both eqs 8 and 5 to calculate the lamellae periodicity. Notably, the planar geometry of the lamellae eliminates curvature-induced dead zones, while the effect of the architecture-induced dead zones decreases upon increasing backbone length, M_i, which justifies application of the SS-SCF model to evaluate the periodicity of the lamellar structures.

https://doi.org/10.1021/acs.macromol.2c00418
Macromolecules XXXX, XXX, XXX–XXX

In Figure 15, the experimentally measured period d_1^{exp} of the lamellae is presented as a function of DP N_A of the PS block. Black squares correspond to positions of the main pick in the SAX scattering intensity curves; white squares with error bars indicate the data from TEM for selected samples. The theoretical values of period $d_1^{theor} = 2(R_1 + D_1)$ were calculated using eq 29, that is, $d_{1,bb}^{theor}$ (blue filled triangles) and $d_{1,cb(m=1)}^{theor}$(blue unfilled triangles) were obtained by treating both blocks either as bottlebrushes or as comblike polymers, respectively. Similarly to the case of the PMMA−PDMS-PMMA triblock copolymer in Figure 14, treatment of the branched blocks as linear chains of impermeable superblobs significantly overestimates the dimensions of microphase-segregated domains, and the experimental and theoretical periods are found in better agreement if the blocks are treated as comblike polymers (see also Figure S5 in SI).

As it follows from Table S2 in the SI, the backbones in both blocks were strongly stretched in the lamellae, particularly at small values of M_i. Nonetheless, the parabolic potential framework SS-SCF reasonably describes the experimental data. Notably, in the theoretical model, the sizes of the monomer units in the backbones and side chains are presumed to be equal. The norbornene monomer unit in the backbone of the PS−PDMS diblock is however approximately two times longer than the monomer units in the PS and PDMS side chains. This difference could be roughly accounted for by assigning $m_i = 2$ in the theoretical estimates of d_1^{theor}. The set of d_1^{theor} for $m_i = 2$ (which doubles the distance between neighboring grafts on the norbornene backbone) is shown in Figure S6 in the SI.

The presented examples of lamellar[13] and spherical[16] mesophases illustrate that treatment of comb-shaped blocks as comblike with $\eta_i = (1 + n_i/m_i)^{1/2}$ leads to a better correspondence between the theoretically predicted and the experimentally measured structural parameters of superstructures. However, such change in treatment of the blocks leads to concomitant relocation of the PS−PDMS and PMMA−PDMS−PMMA series in the morphological diagram presented earlier.[36] Relocation of the PS−PDMS series makes samples with shorter PS side chains ($n_A = 29$) closer to the L−C boundary but still keeps it in the lamellae stability region. All of the PMMA−PDMS-PMMA samples move deeper in the stability region of the spherical morphology. The predicted onset of the cylindrical morphology for a series with $n_B = 14$ (and $\eta_B \approx 3.87$) then significantly decreases compared to the experimental $f_B \approx 0.82$ at which cylindrical PMMA domains were first detected in addition to spherical ones.

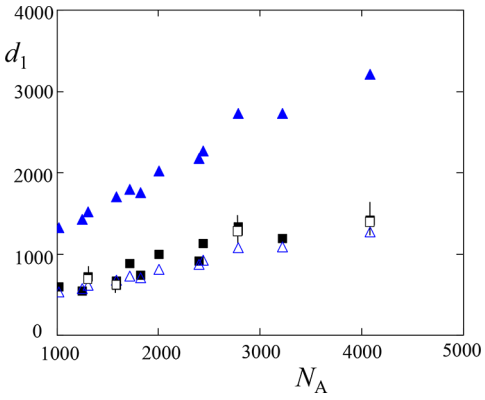

Figure 15. Period d_1(Å) in a microphase-segregated melt of *AB* diblock copolymer PS−PDMD with lamellar morphology ($i = 1$) as a function of DP N_A of PS block. Both blocks constitute molecular brushes: in PS block $n_A = 65$, and in PDMS block $n_B = 29$ or 48 (see Table S2 with data in SI). Experimental values of d_1 (SAXS) are shown by black squares, theoretical values of $d_1 = 2(R_1 + D_1)$ were calculated by treating both blocks as either bottlebrushes with $\eta_i = \alpha_i(l_i b_i)^{3/4} \upsilon_i^{-1/2} n_i^{1/4}$ ($i = A, B$) and numerical coefficients $\alpha_A = 0.65$ and $\alpha_B = 0.5$ (solid blue triangles) or comblike with $\eta_i = (1 + n_i/m_i)^{1/2}$ and $m_i = 1$ (unfilled blue triangles). $\gamma = 0.37$. White squares with error bars are TEM data for selected samples.

7. CONCLUSIONS

In this study, we examined the equilibrium fraction of bridges and the effect of dead zones in microphase-segregated melts of *ABA* block copolymers comprising comb-shaped blocks. The curvature-induced dead zones were described via the two-layer model of the matrix in a Wigner−Seitz cell.

The development of curvature-induced dead zones and variations in the architecture of the *ABA* triblock copolymer affect the fraction of *B* bridges connecting neighboring *A* domains in cylindrical and spherical morphologies (Figures 6 and 7). At a small curvature of the domains (i.e., in the absence of dead zones in the two-layer model), the equilibrium fraction $X_{B,i}$ of the bridges was calculated as in a planar layer. Here, $X_{B,i}$ decreases upon increasing volume fraction f_B of the *B* block due to the increasing difference between the elastic free energies of the loops and bridges.[47] The onset of a dead zone and the increase in its width z_0 upon further increasing f_B lead to progressive accumulation of the median points of the loops closer to the external boundary of the Wigner−Seitz cell, decreasing the difference between the elastic free energies of the loops and bridges. As a result, the equilibrium fraction $X_{B,i}$ of the bridges increases with increasing f_B, passing through a minimum at the onset of the dead zone. An increase in the branching of the central *B* block in the *ABA* block copolymer leads to a reverse effect: the equilibrium fraction of the bridges decreases upon increasing η_B. Although the fraction of bridges, $X_{B,i}$, was estimated using an approximate (two-layer) model of the matrix, the dependence of $X_{B,i}(f_B)$ is expected to remain nonmonotonic in a more rigorous calculation due to the exponential decrease in the width of the dead zone at small curvatures.

We demonstrated that in a wide range of block copolymer compositions, the account of curvature-induced dead zones leads to minor changes in the structural parameters of the domains (Figures 10 and 11) and the positions of the binodals (Figures 8 and 9) compared to the parabolic potential framework SS-SCF used by us previously.[36]

The developed theoretical model invoking linear elasticity of the blocks allows for direct calculation of the domain sizes and interdomain distances in microphase-segregated melts of *AB* and *ABA* block copolymers as a function of DPs of the blocks and their architectural parameters. In spite of the strong elongation of the backbones of the branched blocks in the experimental systems, the structural parameters of the microphase-segregated melts could be still reasonably described by the two-layer model. Deviations between theory and experiments on self-assembling networks of *ABA* copolymers with spherical *A* domains[16,19,49] were moderate when the central *B* block was treated as a comblike polymer.

https://doi.org/10.1021/acs.macromol.2c00418
Macromolecules XXXX, XXX, XXX−XXX

Notably, the discrepancy between theory and experiments could also arise due to the lack of full equilibration of mesophases upon evaporation of nonselective solvent. A good correspondence between theory and experiment was also found for lamellar mesophases formed by *AB* diblock copolymers with comb-shaped blocks[13] when the latter were treated as comblike polymers. Although the backbones in both blocks were strongly stretched, the SS-SCF modeling provided a reasonable description of the lamellae period when the blocks were treated as comblike polymers. We emphasize that in the treatment of comb-shaped blocks as comblike polymers and in a comparison between the theoretical and the experimental data we did not implement adjustable prefactors and used the values of the model parameters reported in the literature.

■ ASSOCIATED CONTENT

Supporting Information

The Supporting Information is available free of charge at https://pubs.acs.org/doi/10.1021/acs.macromol.2c00418.

Detailed derivation of the free energy within a two-layer model for convex dry brushes of comblike macromolecules; analysis of the quantitative effect of the dead zones on the phase diagram for the microphase-separated melt of block copolymers comprising comblike blocks; comparison of the theoretical predictions to experimental data, including tables with experimentally measured structural properties of the copolymers and values of adjustable parameters (PDF)

■ AUTHOR INFORMATION

Corresponding Author

Oleg V. Borisov − *Institute of Macromolecular Compounds of the Russian Academy of Sciences, St. Petersburg 199004, Russia; Institut des Sciences Analytiques et de Physico-Chimie pour l'Environnement et les Matériaux, UMR 5254 CNRS UPPA, Pau 64053, France;* orcid.org/0000-0002-9281-9093; Email: oleg.borisov@uiv-pau.fr

Authors

Ekaterina B. Zhulina − *Institute of Macromolecular Compounds of the Russian Academy of Sciences, St. Petersburg 199004, Russia;* orcid.org/0000-0001-9139-3484

Ivan V. Mikhailov − *Institute of Macromolecular Compounds of the Russian Academy of Sciences, St. Petersburg 199004, Russia*

Complete contact information is available at: https://pubs.acs.org/10.1021/acs.macromol.2c00418

Notes

The authors declare no competing financial interest.

■ ACKNOWLEDGMENTS

This work was supported by the Ministry of Research and Education of the Russian Federation within State Contract No. 14.W03.31.0022.

■ REFERENCES

(1) Wurm, F.; Frey, H. Linear-dendritic block copolymers: the state of the art and exciting perspectives. *Prog. Polym. Sci.* **2011**, *36*, 1−52.

(2) Blasco, E.; Pinol, M.; Oriol, L. Responsive Linear-Dendritic Block Copolymers. *Macromol. Rapid Commun.* **2014**, *35* (12), 1090−1115.

(3) Garcia-Juan, H.; Nogales, A.; Blasco, E.; Martinez, J. C.; Sics, I.; Ezquerra, T. A.; Pinol, M.; Oriol, L. Self-assembly of thermo and light responsive amphiphilic linear dendritic block copolymers. *Eur. Polym. J.* **2016**, *81*, 621−633.

(4) Mirsharghi, S.; Knudsen, K. D.; Bagherifam, S.; Nystrom, B.; Boas, U. Preparation and self-assembly of amphiphilic polylysine dendrons. *New J. Chem.* **2016**, *40*, 3597−3611.

(5) Fan, X.; Zhao, Y.; Xu, W.; Li, L. Linear-Dendritic Block Copolymer for Drug and Gene Delivery. *Mater. Sci. Eng., C* **2016**, *62*, 943−959.

(6) Rzayev, J. Synthethis of polystyrene-polylactide bottlebrush block copolymers and their melt self-assembly into large domain nanostructures. *Macromolecules* **2009**, *42*, 2135−2141.

(7) Liberman-Martin, A. L.; Chu, C. K.; Grubbs, R. H. Application of Bottlebrush Block Copolymers as Photonic Crystals. *Macromol. Rapid Commun.* **2017**, *38*, 1700058.

(8) Song, D. P.; Zhao, T. H.; Guidetti, G.; Vignolini, S.; Parker, R. M. Hierarchical Photonic Pigments via the Confined Self-Assembly of Bottlebrush Block Copolymers. *ACS Nano* **2019**, *13*, 1764−1771.

(9) Bolton, J.; Bailey, T. S.; Rzayev, J. Large pore size nanoporous materials from self-assembly of asymmetric bottlebrush block copolymers. *Nano Lett.* **2011**, *11*, 998−1001.

(10) Gai, Y.; Song, D.-P.; Yavitt, B. M.; Watkins, J. J. Polystyrene-block-poly(ethylene oxide) Bottlebrush Block CopolymerMorphology Transitions: Influence of Side Chain Length and Volume Fraction. *Macromolecules* **2017**, *50*, 1503−1511.

(11) Runge, M. B.; Bowden, N. B. Synthesis of High Molecular Weight Comb Block Copolymers and Their Assembly into Ordered Morphologies in the Solid State. *J. Am. Chem. Soc.* **2007**, *129*, 10551−10560.

(12) Runge, M. B.; Lipscomb, C. E.; Ditzler, L. R.; Mahanthappa, M. K.; Tivanski, A. V.; Bowden, N. B. Investigation of the Assembly of Comb Block Copolymers in the Solid State. *Macromolecules* **2008**, *41*, 7687−7694.

(13) Fei, H.-F.; Yavitt, B. M.; Hu, X.; Kopanati, G.; Ribbe, A.; Watkins, J. J. Influence of Molecular Architecture and Chain Flexibility on the Phase Map of Polystyrene-block-poly(dimethylsiloxane) Brush Block Copolymers. *Macromolecules* **2019**, *52*, 6449−6457.

(14) Sunday, D. F.; Chang, A. B.; Liman, C. D.; Gann, E.; Delongchamp, D. M.; Thomsen, L.; Matsen, M. W.; Grubbs, R. H.; Soles, C. L. Self-Assembly of ABC Bottlebrush Triblock Terpolymers with Evidence for Looped Backbone Conformations. *Macromolecules* **2018**, *51* (18), 7178−7185.

(15) Bolton, J.; Rzayev, J. Synthesis and Melt Self-Assembly of PS-PMMA-PLA Triblock Bottlebrush Copolymers. *Macromolecules* **2014**, *47*, 2864−2874.

(16) Vatankhah-Varnosfaderani, M.; Keith, A. N.; Cong, Y.; Liang, H.; Rosenthal, M.; Sztucki, M.; Clair, C.; Magonov, S.; Ivanov, D. A.; Dobrynin, A. V.; Sheiko, S. S. Chameleon-like elastomers with molecularly encodded strain-adaptive stiffening and coloration. *Science* **2018**, *359*, 1509−1513.

(17) Yuan, J.; Müller, A. H. E.; Matyjaszewski, K.; Sheiko, S. In *Polymer Science: A Comprehensive Reference*; Matyjaszewski, K., Möller, M., Eds.; Elsevier: Amsterdam, 2012.

(18) Tu, S.; Choudhury, C. K.; Luzinov, I.; Kuksenok, O. Recent advances towards applications of molecular bottlebrushes and their conjugates. *Curr. Opin. Solid State Mater. Sci.* **2019**, *23*, 50.

(19) Xie, G.; Martinez, M. R.; Olszewski, M.; Sheiko, S. S.; Matyjaszewski, K. Molecular Bottlebrushes as Novel Materials. *Biomacromolecules* **2019**, *20* (1), 27−54.

(20) Gillich, T.; Benetti, E. M.; Rakhmatullina, E.; Konradi, R.; Li, W.; Zhang, A.; Schlüter, A. D.; Textor, M. Self-Assembly of Focal Point Oligo-Catechol Ethylene Glycol Dendrons on Titanium Oxide Surfaces: Adsorption Kinetics, Surface Characterization, and Non-fouling Properties. *J. Am. Chem. Soc.* **2011**, *133*, 10940−10950.

https://doi.org/10.1021/acs.macromol.2c00418
Macromolecules XXXX, XXX, XXX−XXX

(21) Yeh, P. Y. J.; Kainthan, R. K.; Zou, Y.; Chiao, M.; Kizhakkedathu, J. N. Self-assembled monothiol-terminated hyperbranched polyglycerols on a gold surface: a comparative study on the structure, morphology, and protein adsorption characteristics with linear poly(ethylene glycol). *Langmuir* **2008**, *24*, 4907−4916.
(22) Gillich, T.; Acikgoz, C.; Isa, L.; Schluter, A. D.; Spencer, N. D.; Textor, M. PEG-Stabilized Core-Shell Nanoparticles: Impact of Linear versus Dendritic Polymer Shell Architecture on Colloidal Properties and the Reversibility of Temperature-Induced Aggregation. *ACS Nano* **2013**, *7*, 316−329.
(23) Pickett, G. T. Classical Path Analysis of end-Grafted Dendrimers: Dendrimer Forest. *Macromolecules* **2001**, *34*, 8784−8791.
(24) Zook, T. C.; Pickett, G. T. Hollow-Core Dendrimers Revised. *Physical review letters* **2003**, *90* (1), 015502.
(25) Kröger, M.; Peleg, O.; Halperin, A. From Dendrimers to Dendronized Polymers and Forests: Scaling Theory and its Limitations. *Macromolecules* **2010**, *43*, 6213−6224.
(26) Gergidis, L. N.; Kalogirou, A.; Vlahos, C. Dendritic Brushes under Good Solvent Conditions: A Simulation Study. *Langmuir* **2012**, *28*, 17176−17185.
(27) Polotsky, A. A.; Gillich, T.; Borisov, O. V.; Leermakers, F. A. M.; Textor, M.; Birshtein, T. M. Dendritic versus Linear Polymer Brushes: Self-Consistent Field Modelling, Scaling Theory, and Experiment. *Macromolecules* **2010**, *43*, 9555−9566.
(28) Borisov, O. V.; Polotsky, A. A.; Rud, O. V.; Zhulina, E. B.; Leermakers, F. A. M.; Birshtein, T. M. Dendron Brushes and Dendronized Polymers: A Theoretical Outlook. *Soft Matter* **2014**, *10*, 2093−2101.
(29) Li, C.-W.; Merlitz, H.; Wu, C.-X.; Sommer, J.-U. The structure of brushes made of dendrimers: Recent Advances. *Polymer* **2016**, *98*, 437−447.
(30) Leermakers, F. A. M.; Zhulina, E. B.; Borisov, O. V. Interaction forces and lubrication of dendronized surfaces. *Curr. Opin. Colloid Interface Sci.* **2017**, *27*, 50−56.
(31) Polotsky, A. A.; Leermakers, F. A. M.; Zhulina, E. B.; Birshtein, T. M. On the Two-Population Structure of Brushes Made of Arm-Grafted Polymer Stars. *Macromolecules* **2012**, *45*, 7260−7273.
(32) Zhulina, E. B.; Leermakers, F. A. M.; Borisov, O. V. Theory of brushes formed by Ψ-shaped macromolecules at solid-liquid interfaces. *Langmuir* **2015**, *31* (23), 6514−6522.
(33) Lebedeva, I. O.; Zhulina, E. B.; Borisov, O. V. Theory of Linear-dendritic Block Copolymer Micelles. *ACS Macro Lett.* **2018**, *7* (1), 42−46.
(34) Lebedeva, I. O.; Zhulina, E. B.; Leermakers, F. A. M.; Borisov, O. V. Dendron and Hyperbranched Polymer Brushes in Good and Poor Solvents. *Langmuir* **2017**, *33*, 1315−1325.
(35) Borisov, O. V.; Zhulina, E. B.; Polotsky, A. A.; Leermakers, F. A. M.; Birshtein, T. M. Interactions between Brushes of Root-tethered Dendrons. *Macromolecules* **2014**, *47* (19), 6932−6945.
(36) Zhulina, E. B.; Sheiko, S. S.; Dobrynin, A. V.; Borisov, O. V. Microphase segregation in the melts of bottlebrush block copolymers. *Macromolecules* **2020**, *53* (7), 2582−2593.
(37) Semenov, A. N. Contribution to the Theory of Microphase Layering in Block-Copolymer Melts. *Sov. Phys. JETP* **1985**, *61*, 733−742.
(38) Ball, R. C.; Marko, J. F.; Milner, S. T.; Witten, T. A. Polymers Grafted to a Convex Surface. *Macromolecules* **1991**, *24*, 693−703.
(39) Belyi, V. A. Exclusion Zone of Convex Brushes in the Strong-Streching Limit. *J. Chem. Phys.* **2004**, *121*, 6547.
(40) Dimitriev, M. S.; Grason, G. M. End-exclusion zones in strongly stretched, molten polymer brushes of arbitrary shape. *J. Chem. Phys.* **2021**, *155*, 224901.
(41) Wijmans, C. M.; Zhulina, E. B. Polymer Brushes at Curved Surfaces. *Macromolecules* **1993**, *26* (26), 7214−7224.
(42) Park, S. J.; Cheong, G. K.; Bates, F. S.; Dorfman, K. D. Stability of the Double Gyroid Phase in Bottlebrush Diblock Copolymer Melts. *Macromolecules* **2021**, *54*, 9063−9070.
(43) Rud, O. V.; Polotsky, A. A.; Gillich, T.; Borisov, O. V.; Leermakers, F. A. M.; Textor, M.; Birshtein, T. M. Dendritic Spherical Polymer Brushes: Theory and Self-Consistent Field Modelling. *Macromolecules* **2013**, *46*, 4651−4662.
(44) Tian, Y.; Ina, M.; Cao, Z.; Sheiko, S. S.; Dobrynin, A. V. How to Measure Work of Adhesion and Surface Tension of Soft Polymeric Materials. *Macromolecules* **2018**, *51* (11), 4059−4067.
(45) Mikhailov, I. V.; Zhulina, E. B.; Borisov, O. V. Brushes and lamellar mesophases of comb-shaped (co)polymers: a self-consistent field theory. *Phys. Chem. Chem. Phys.* **2020**, *22*, 23385−23398.
(46) Fleer, G. J.; Cohen Stuart, M. A.; Scheutjens, J. M. H. M.; Cosgrove, T.; Vincent, B. *Polymers at Interfaces*; Chapman & Hall: London, 1993.
(47) Mikhailov, I. V.; Leermakers, F. A. M.; Darinskii, A. A.; Zhulina, E. B.; Borisov, O. V. Theory of microphase segregation in ABA triblock comb-shaped copolymers: lamellar mesophase. *Macromolecules* **2021**, *54*, 4747−4759.
(48) Zhulina, E. B.; Leermakers, F. A. M.; Borisov, O. V. Brushes of Cycled Macromolecules: Structure and Lubricating Properties. *Macromolecules* **2016**, *49* (22), 8758−8767.
(49) Clair, C.; Lallam, A.; Rosenthal, M.; Sztucki, M.; Vatankhah-Varnosfaderani, M.; Keith, A. N.; Cong, Y.; Liang, H.; Dobrynin, A. V.; Sheiko, S. S.; Ivanov, D. A. Strained Bottlebrushes in Super-Soft Physical Networks. *ACS Macro Lett.* **2019**, *8* (5), 530−534.
(50) Liang, H.; Wang, Z.; Dobrynin, A. V. Strain-Adaptive Self-Assembled Networks of Linear-Bottlebrush-Linear Copolymers. *Macromolecules* **2019**, *52*, 8617−8624.
(51) Wessels, M. J.; Jayaraman, A. Molecular dynamic simulation study of linear, bottlebrush, and star-like amphiphilic block polymer assembly in solution. *Soft Matter* **2019**, *15*, 3987−3998.
(52) Paturej, J. J.; Sheiko, S. S.; Panyukov, S.; Rubinstein, M. Molecular Structure of Bottlebrush Polymers in Melts. *Science Advances* **2016**, *2* (11), No. e1601448.

https://doi.org/10.1021/acs.macromol.2c00418
Macromolecules XXXX, XXX, XXX−XXX